3-2005

Modeling the Infrared Intensity of a Large Commercial Aircraft

Ruben Martinez

**MODELING THE INFRARED INTENSITY OF A LARGE COMMERICAL
AIRCRAFT**

THESIS

Ruben Martinez, Captain, USAF

AFIT/GE/ENP/05-01

DEPARTMENT OF THE AIR FORCE

AIR UNIVERSITY

AIR FORCE INSTITUTE OF TECHNOLOGY

Wright-Patterson Air Force Base, Ohio

MODELING THE INFRARED INTENSITY OF A LARGE COMMERICAL AIRCRAFT

THESIS

Presented to the Faculty

Department of Engineering Physics

Graduate School of Engineering and Management

Air Force Institute of Technology

Air University

Air Education and Training Command

in Partial Fulfillment of the Requirements for the

Degree of Master of Science in Electrical Engineering

Ruben Martinez, BSEE

Captain, USAF

March 2005

AFIT/GE/ENP/05-01

**MODELING THE INFRARED INTENSITY OF A LARGE COMMERICAL
AIRCRAFT**

Ruben Martinez, BSEE
Captain, USAF

Approved:
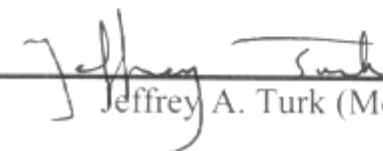

_____   _3 Mar 05_____
Michael A. Marciniak (Chairman)   date

_____   _3 May 05_____
Robert L. Hengehold (Member)   date

_____   _7 Mar 05_____
Jeffrey A. Turk (Member)   date

Abstract

Measuring the infrared signature of large civilian aircraft has become increasingly important due to the proliferation of man-portable air defense systems (MANPADS) and the increasing threat of their use by terrorists. Because of the range of these shoulder-fired weapons, most aircraft flying over 20,000 feet are safe from the threat; however, aircraft taking-off or landing are extremely vulnerable.

A radiometric model was developed to simulate a large commercial aircraft's infrared intensity during these two critical phases of flight. The radiometric model was largely based on the dimensions of a Boeing 747-400 aircraft. It is capable of simulating elevation angles between -20º and +20º, as well as 360º in azimuth in its projected area analysis of the faceted model. The model utilizes an obscuration matrix to determine which parts of the aircraft are in view by the observer and thus contribute to the aircraft's intensity. A simple one-bounce reflection matrix was also included to incorporate reflections of hot parts off other body parts, as well as earth- and sky-shine contributions to the overall intensity. Various atmospheric scenarios can be loaded into the model to incorporate atmospheric transmittance and radiance effects in the simulation. Measurements taken at the Air Force Research Laboratory's Optical Measurement Facility are used to create material matrices which account for angle-dependent emissivity and reflectance.

A graphical user interface (GUI) was developed to allow a user to change variables and view the resultant aircraft intensity as a function of elevation and azimuth

angles. A graphical output of the faceted model assists in visualizing aircraft hot parts, reflections, and/or obstructed parts to identify significant contributions to the aircraft's infrared intensity.

Table of Contents

List of Figures

List of Tables

MODELING THE INFRARED INTENSITY OF A LARGE COMMERICAL AIRCRAFT

I Introduction

1.1 The Threat of Infrared-Guided Missiles against Civilian Aircraft

Since its advent in the early 1950's, the infrared (IR)-guided missile has been the most effective anti-aircraft weapon developed. From the Vietnam conflict through Operation Desert Storm, IR missiles have shot down more aircraft than any other anti-aircraft system [21]. The IR missile effectiveness was clearly demonstrated in the 1994-1996 Chechnyan war, where 40% to 60% of aircraft losses were attributed to IR missile strikes [12]. Its proven record against military aircraft also makes the IR-guided missile a serious terrorist threat to commercial aircraft.

The type of surface-to-air missile (SAM) most likely to be employed against commercial aircraft is the man-portable air defense system (MANPADS), also known as a shoulder-fired missile. MANPADS are lightweight, transportable, inexpensive, and fully capable of striking both military aircraft and commercial airliners. These systems have reportedly been proliferated over the years due to the breakup of the Soviet Union in the early 1990's and even US support of the Mujahideen in Afghanistan in the 1980's [16], [19]. These proliferated systems have already been used against civilian aircraft. Over the past 25 years, there have been 35 shoulder-fired missile attacks on civilian aircraft. Of these attacks, 24 resulted in crashes with 500 fatalities [10].

Recent events are clear evidence that terrorists are willing and capable of using IR-guided missiles against civilian aircraft. For example, in June 2002, a missile tube from a Soviet-made SA-7 was discovered near the perimeter of Prince Sultan Air Base, a US Air Force base in Saudi Arabia [14]. The missile had apparently been launched, but no US aircraft were struck. In November of the same year, two shoulder-fired IR-guided missiles were launched against an Arkia Boeing 757 carrying over 270 Israeli passengers from Mombasa, Kenya [18]. Luckily for those on board, the missiles missed the airplane. In August 2003, a Briton was arrested for attempting to smuggle a Russian-made SA-18 MANPAD into the US for the purpose of shooting down a commercial airliner [3]. Most recently in November 2003, a DHL Airbus A300B4-200 freighter was struck by a SA-7 heat-seeking missile while departing Baghdad International Airport [11]. The aircraft lost hydraulic controls, but was able to land thanks to the well-trained pilots. These events show the progression from attempted strikes, to near-hits, and lastly to a successful strike. These only represent the civilian cases that made the news. There are various reports of military aircraft (mainly helicopters) being downed in Iraqi operations, but details are sparse [2].

In May of 2003, the Department of Homeland Security submitted a plan to Congress detailing the implementation of an anti-missile system on a single commercial aircraft type within two years [2]. Fiscal year 2004 funding of the program was approved by The Department of Homeland Security Appropriations Act for 2004. Consequently, Congress granted $60 million for development and testing of an IR countermeasure system. Funding for installation of these systems on the commercial fleet is still a source of contention and has yet to be appropriated. In a separate effort called the Large Aircraft

Survivability Initiative (LASI), the United States Air Force is exploring ways commercial aircraft can be hardened to improve their chances of surviving a missile strike. Both the Department of Homeland Security and the US Air Force view the IR missile as a formidable terrorist threat to commercial aircraft.

1.2   Thesis Overview

1.2.1   Purpose

The objective of this thesis is to develop a desktop tool that is capable of identifying IR signature trends of a large commercial aircraft. Once these trends have been identified, planners can focus their use of robust IR codes to more precisely evaluate vulnerabilities.

1.2.2   Organization

Chapter I, just presented, highlights the increasing threat to commercial aircraft providing the impetus for this thesis. Chapter II covers radiometry fundamentals and presents the dimensions of the Boeing Commercial Aircraft 747-400 which serves as the basis for the faceted model (sometimes referred to as a wire-frame model). In Chapter III, a short introduction to 3-D modeling in MATLAB® is followed by a description of how the faceted model was created and errors associated with facetization.   The obscuration and reflection matrices and their functions in the radiometric model are then introduced. The effects of aircraft surface properties and atmospheric conditions are then explored. Chapter III concludes with the radiometric calculations at the heart of the radiometric model. The graphical user interface (GUI) makes the radiometric model a useful desktop tool and is discussed in Chapter IV. Several examples of how the

radiometric model is exercised using the GUI are presented. Chapter V concludes the

thesis and lists recommendations for future work.

II Background

2.1 Overview

Fundamental radiometric concepts incorporated in this thesis are outlined in this chapter. Blackbody radiation theory, emissivity, and reflectance are extensively used in the radiometric model. The relationship between emissivity and reflectance given by Kirchoff's Law is important since reflectance measurements are easier, and thus more common, than emissivity measurements. Chapter II concludes with the selection of the Boeing 747-400 as the basis for the faceted model.

2.2 Radiometry Review

2.2.1 Infrared Spectrum

All matter in the known universe absorbs and re-emits energy unless it is at a temperature of absolute zero (0 K). The energy emitted by this matter is in the form of electromagnetic radiation, which can be arranged by its wavelength or frequency within the electromagnetic spectrum. The portion of the spectrum bounded by visible light on one side and microwaves on the other is called the *infrared* spectrum. Since heated objects radiate in the infrared, the terms *heat* and *infrared* are sometimes used interchangeably[1] [9]. The prefix *infra* is derived from the Latin word meaning *below*. *Infrared*, it follows, means *below red* and has a lower frequency than red visible light. Figure 2-1 depicts a portion of the electromagnetic spectrum including the infrared region which spans from approximately 0.7-1000 microns (μm). The IR spectrum is divided into five regions: the shortwave infrared region (SWIR) from 0.7-3 μm, midwave

---

[1] The object need only be at a finite temperature greater than absolute zero.
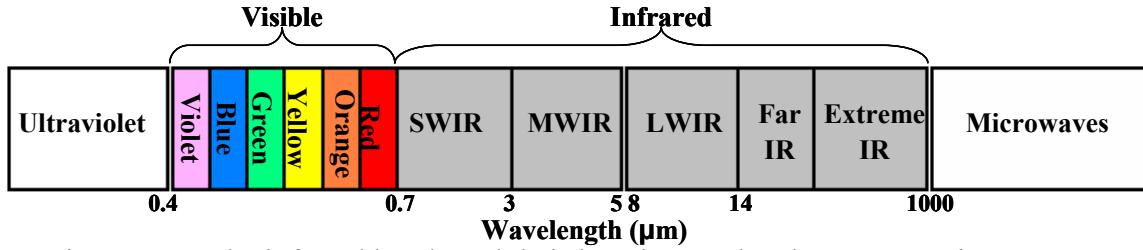
Figure 2-1: The infrared bands and their location on the electromagnetic spectrum.

infrared region (MWIR) from 3-5 μm, longwave infrared region (LWIR) from 8-14 μm, and the Far/Extreme IR regions from 14-1000 μm. Infrared radiation in the region from 5-8 μm is generally excluded from the spectrum since IR signals in this band are severely attenuated by the atmosphere and provide no detection capability. This thesis will focus on the 3-5 μm and 8-12 μm ranges and refer to them as the midwave and longwave bands, respectively.

2.2.2   Terminology [2]

One of the most significant properties of the electromagnetic wave is that it can transport energy, which is measured in joules (J) [8]. The time rate of change of energy (J/s) is measured in watts (W) and is referred to as radiant *flux* (Φ_e). The radiometric terms and their units are presented in Table 2-1. Of these terms, *radiance* (L_e), is perhaps the most versatile of all and is defined as the flux emitted by an extended source[3] per unit projected source area ($A_s \cdot \cos \theta_s$) per unit solid angle[4] (Ω_d).

---

[2] Only *energy-derived* terms (based on the joule as the fundamental quantity) are discussed. *Photon-derived* terms (based on the number of photons) are not discussed.

[3] An extended source is one that has appreciable area compared to the square of the distance from the source.

[4] The solid angle is measured in steradians (sr) and is the ratio of an area on the surface of a sphere to the square of the radius: $\Omega = A/r^2$ [6].

Table 2-1: The energy-derived radiometric terms and their respective units.

Symbol	Quantity	Units
Q_e	Energy	joule
Φ_e	Flux	watt
I_e	Intensity	watt·sr^{-1}
E_e	Irradiance	watt·cm^{-2}
M_e	Exitance	watt·cm^{-2}
L_e	Radiance	watt·cm^{-2}sr^{-1}

Radiance has units of W·cm^{-2}·steradian^{-1} and is given in differential form by

$$L_e = \frac{\partial^2 \Phi_e}{\partial A_s \cos \theta_s \partial \Omega_d},$$ (Eq 2-1)

where

$$\partial \Omega_d = \partial A_d \cos \theta_d / R^2 .$$ (Eq 2-2)

The distance from the source to the detector is R and the area of the detector is A_d. The angles subtended from the line connecting the source and detector to the normals of both the source and detector are θ_s and θ_d, respectively. Figure 2-2 illustrates these angles, as
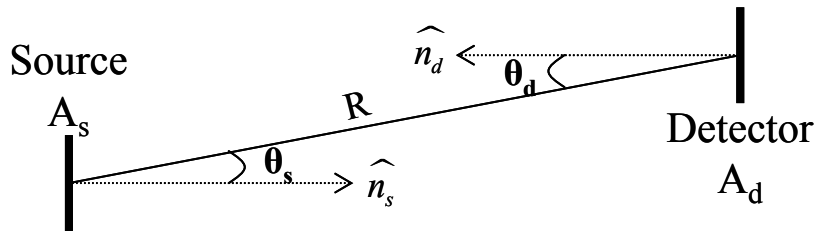
Figure 2-2: Angles and distances used in radiometric calculations

well as the distance between the source and detector, R. The other radiometric terms can easily be derived from Equation (2-1). For example, the equation can be rearranged to solve for differential flux, $\partial^2\Phi_e$,

$$\partial^2\Phi_e = L_e\partial A_s\cos\theta_s\partial\Omega_d .$$ (Eq 2-3)

By integrating both sides twice, the total flux is derived:

$$\Phi_e = \int_{A_s}\int_{\Omega_d} L_e\cos\theta_s dA_s d\Omega_d .$$ (Eq 2-4)

Flux is synonymous with power and can either be emitted by a surface or incident on a surface. To distinguish between the two cases, there are two respective terms: *exitance* (M_e) and *irradiance* (E_e), both of which have units of W·cm^{-2}. Exitance (M_e) is the flux emitted per unit source area into a hemisphere of 2π steradians and can be found by substituting for $\partial\Omega_d$ from Equation (2-2), rearranging Equation (2-4), and then integrating with respect to the differential detector area:

$$M_e = \frac{\partial\Phi_e}{\partial A_s} = \int_{\Omega_d} L_e\cos\theta_s d\Omega_d = \int_{A_d}\frac{L_e}{R^2}\cos\theta_s\cos\theta_d dA_d .$$ (Eq 2-5)

Irradiance (E_e) is the flux received per unit detector and is similarly derived from Equation (2-4), integrating with respect to the differential source area instead:

$$E_e = \frac{\partial\Phi_e}{\partial A_d} = \int_{A_s}\frac{L_e}{R^2}\cos\theta_s\cos\theta_d dA_s .$$ (Eq 2-6)

The source is considered a point source if its area is not significant with respect to the square of the distance to the detector ($A_s \ll R^2$). The radiometric term to quantify flux

from a point source is *intensity* (I_e). Intensity can be thought of as flux per unit solid

angle (W·steradian^{-1}) and is calculated from Equation (2-4) by rearranging and then

integrating with respect to the source area.

$$I_e = \frac{\partial \Phi_e}{\partial \Omega_d} = \int_{A_s} L_e \cos\theta_s dA_s \qquad \text{(Eq 2-7)}$$

If the area of the source and detector are both much smaller than the distance

between them squared ($A_s, A_d << R^2$) and the detector is oriented with its normal along the

line connecting it to the source ($\theta_d \approx 0$), then Equations (2-1) through (2-7) simplify as

follows, respectively:

$$L_e \cong \frac{\Phi_e}{\Omega_d A_s \cos\theta_s}, \qquad \text{(Eq 2-8)}$$

$$\Omega_d \cong \frac{A_d}{R^2}, \qquad \text{(Eq 2-9)}$$

$$\Phi_e \cong L_e \Omega_d A_s \cos\theta_s, \qquad \text{(Eq 2-10)}$$

$$M_e \cong \frac{\Phi_e}{A_s} \cong \frac{L_e A_d}{R^2} \cos\theta_s, \qquad \text{(Eq 2-11)}$$

$$E_e \cong \frac{\Phi_e}{A_d} \cong \frac{L_e A_s}{R^2} \cos\theta_s, \qquad \text{(Eq 2-12)}$$

$$I_e \cong \frac{\Phi_e}{\Omega_d} \cong L_e A_s \cos\theta_s. \qquad \text{(Eq 2-13)}$$

An assumption often used in radiometric problems is that sources are *Lambertian* radiators, whose radiance is independent of view angle, θ_s[5]. Lambertian sources can also be thought of as perfectly diffuse sources. Equation (2-14) provides the relationship between exitance and radiance for a planar, Lambertian source [6].

$$M_e = \pi L_e \qquad \text{(Eq 2-14)}$$

The radiance, exitance, and irradiance terms presented thus far are independent of the infrared radiation wavelength (λ). In reality, the quantities are spectral in nature – that is, they are not distributed uniformly over all wavelengths. The following section will specifically discuss the spectral nature of exitance.

2.2.3 Blackbody Radiation Theory

A blackbody is a perfect radiator and emits the maximum number of photons per unit time from a surface area in a wavelength interval that any body can radiate at a given kinetic temperature [6]. Any surface in thermodynamic equilibrium cannot radiate more photons than a blackbody unless it contains fluorescent or radioactive materials. The blackbody is the ultimate thermal radiator and provides a benchmark to which any other source may be compared.

The radiant properties of blackbodies are described by *Planck's Radiation Law*, which evaluates the spectral[6] exitance of a blackbody at a given temperature as follows:

$$M_e(\lambda, T) = \frac{2\pi hc^2}{\lambda^5 \left(e^{hc/\lambda kT} - 1\right)}, \qquad \text{(Eq 2-15)}$$

---

[5] Equation (2.1) still shows radiance dependent on $\cos \theta_s$; however, this is due to the *projected area* term, $A_s \cdot \cos \theta_s$, and not a direct dependence on θ_s (i.e., non-Lambertian implies $L_e(\theta_s)$).
[6] Spectral implies as a function of wavelength.

where λ is the wavelength in microns (μm), T is the temperature in Kelvin (K), h is Planck's constant ($\approx 6.63 \times 10^{-34}$ J·s), k is Boltzmann's constant ($\approx 1.38 \times 10^{-23}$ J·K^{-1}), and c is the speed of light ($\approx 3.00 \times 10^{8}$ m·s^{-1}). Since a blackbody is perfectly Lambertian, Equation (2-14) implies that its radiance is simply the exitance divided by π, or:

$$L_e(\lambda,T) = \frac{2hc^2}{\lambda^5\left(e^{hc/\lambda kT} - 1\right)}.$$
(Eq 2-16)

Figure 2-3 shows the blackbody exitance curves as described in Equation (2-15) for temperatures varying from 1000-1500 K. Figure 2-3 also illustrates a decrease in the wavelength of peak exitance with an increase in temperature. The relationship between the wavelength of peak exitance and temperature can be found by setting the partial
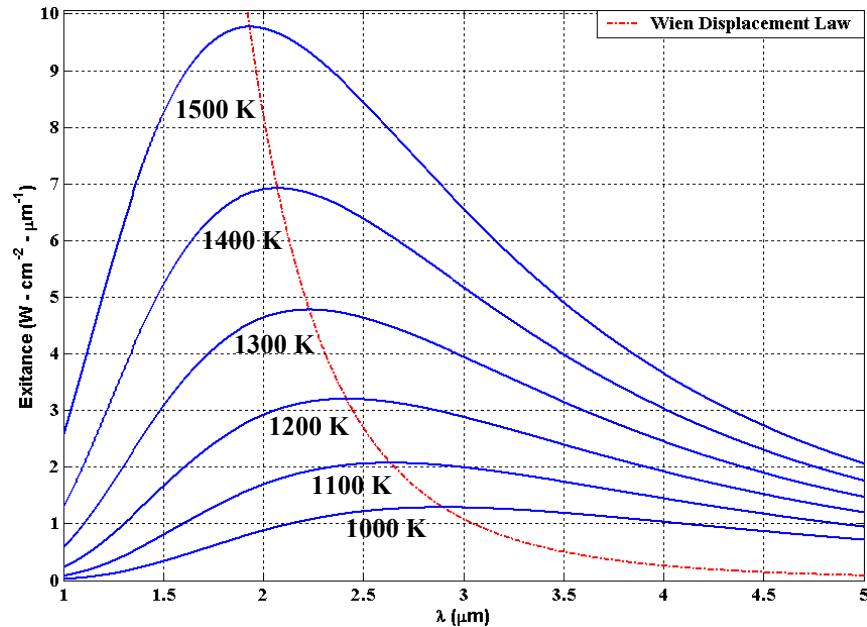
Figure 2-3: The solid lines represent the blackbody curves for varying temperatures. The broken line is the Wien's Law hyperbola and intersects the blackbody curves at the exitance peaks.

derivative of Equation (2-15) to zero and solving for wavelength at maximum exitance:

$$\frac{\partial M_e(\lambda, T)}{\partial \lambda} = 0 .$$ (Eq 2-17)

The result is termed the *Wien Displacement Law* [6],

$$\lambda_{max} = \frac{2898(\mu mK)}{T(K)} ,$$ (Eq 2-18)

and is depicted in Figure 2-3 as a hyperbola crossing each of the exitance peaks. Equation (2-18) can be rearranged to solve for temperature, allowing one to easily calculate the temperature of the blackbody given its peak wavelength from its blackbody curve.

To find the total exitance from a blackbody at a temperature, T, Equation (2-15) is integrated over all wavelengths as shown in Equation 2-19.

$$M_e(T) = \int_0^\infty \frac{2\pi hc^2}{\lambda^5 \left(e^{hc/\lambda kT} - 1\right)} d\lambda .$$ (Eq 2-19)

The resulting expression from the integration in Equation 2-19,

$$M_e(T) = \sigma_e T^4 ,$$ (Eq 2-20)

is known as the *Stefan-Boltzmann Law* where σ_e ($\approx 5.67 \times 10^{-12}$ W·cm^{-2}·K^{-4}) is the Stefan-Boltzman constant.

While ideal blackbodies are useful in comparisons and near-ideal blackbodies are often used for calibration, real sources radiate differently than blackbodies. Therefore, real sources must be characterized in terms of their emissivity.

2.2.4 Emissivity

Emissivity, ε, is the measure of how closely the spectral exitance of a real source corresponds to that of a blackbody. Since the blackbody represents the ideal, then true exitance of any non-blackbody source cannot exceed the blackbody curve at the same temperature as the source. Therefore, emissivity is a dimensionless quantity with the following constraint: $0 \leq \varepsilon \leq 1$. Quantitatively, emissivity is defined as the ratio of the spectral exitance of the actual source and the spectral exitance of a blackbody at the same temperature:

$$\varepsilon(\lambda,T) = \frac{M_e(\lambda,T)_{source}}{M_e(\lambda,T)_{blackbody}} . \qquad \text{(Eq 2-21)}$$

A blackbody has an emissivity of one, whereas a real source will have an emissivity of less than one. If the emissivity of a real source is independent of wavelength, then that source is called a graybody and Equation (2-21) can be re-written as:

$$\varepsilon(T) = \frac{M_e(\lambda,T)_{graybody}}{M_e(\lambda,T)_{blackbody}} . \qquad \text{(Eq 2-22)}$$

The spectral exitance curve for a graybody will follow that of a blackbody of the same temperature, but will be scaled by the emissivity. Realistically, there are no true graybody sources; however, over particular IR bands, some sources act as a graybody. At the IR bands being considered by this thesis, the aircraft surface is treated as a graybody with a dependence on the angle of incidence as discussed in Chapter III.

If the emissivity of a source is dependent on wavelength (ε (λ)), then that source is called a selective radiator. The spectral exitance curve for a selective radiator will still be bounded by the spectral exitance curve of a blackbody, but may not have the same shape as the blackbody curve. A comparison of spectral exitance curves between a blackbody, graybody, and selective radiator at 1000 K is illustrated in Figure 2-4. Note that the blackbody and graybody curves peak at the same wavelength. The graybody and selective emitter shown are bounded by the blackbody curve. Equation (2-21) can be rearranged to find the spectral exitance of a real source:

$$M_e(\lambda,T)_{source} = \varepsilon(\lambda,T) \cdot M_e(\lambda,T)_{blackbody} = \varepsilon(\lambda,T) \frac{2\pi hc^2}{\lambda^5 \left(e^{hc/\lambda kT} - 1\right)}. \qquad \text{(Eq 2-23)}$$
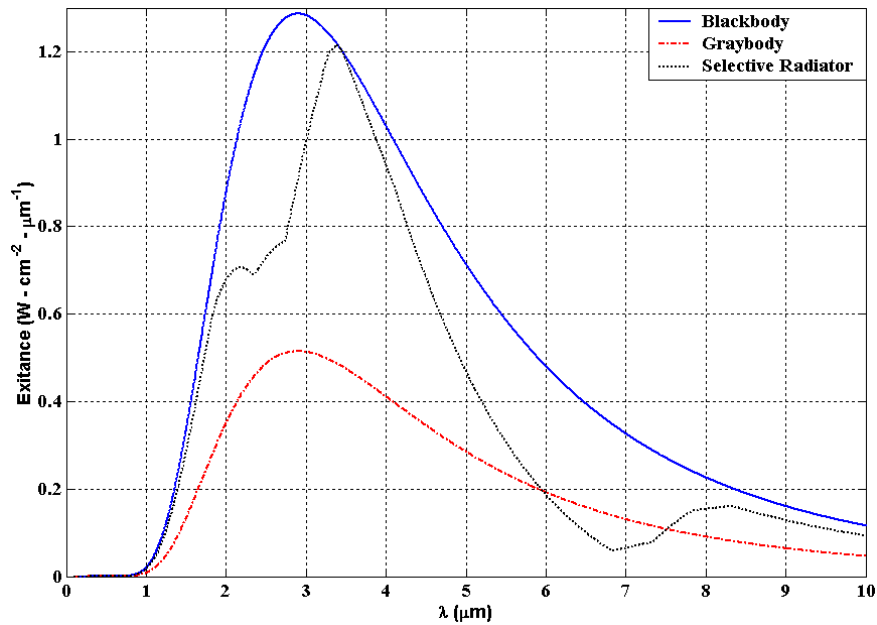
Figure 2-4: The curve with the highest peak is the spectral exitance curve for a blackbody at 1000 K. The irregularly shaped curve is that for a selective radiator. The selective radiator exhibits different emissivities for different wavelength bands. The graybody curve follows that of the blackbody, but is scaled by the emissivity (0.6 in this case).

To find total exitance of the real source, one must integrate over all wavelengths:

$$M_e(T) = \int_0^\infty \varepsilon(\lambda,T) \frac{2\pi hc^2}{\lambda^5 \left(e^{hc/\lambda kT}-1\right)} d\lambda \; .$$ (Eq 2-24)

If the source is a graybody, the emissivity term is not a function of wavelength and can be factored out of the integral. The integral without the emissivity term is simply the Stefan-Boltzmann Law and so the total exitance for the graybody is:

$$M_{e\,gb}(T) = \varepsilon \sigma_e T^4 \; .$$ (Eq 2-25)

Obviously, since emissivity for a graybody is less than one, its total exitance will always be less than that of a blackbody at the same temperature. Recall from Section 2.2.1, this thesis will focus on the 3-5 μm and 8-12 μm bands. As a result, the Stefan-Boltzmann Law is not practical for this thesis. Instead, exitance will be computed over the band of interest. Therefore, Equation (2-23) becomes

$$M_e(T) = \int_{\lambda_1}^{\lambda_2} \varepsilon(\lambda,T) \frac{2\pi hc^2}{\lambda^5 \left(e^{hc/\lambda kT}-1\right)} d\lambda$$ (Eq 2-26)

.

Section 3.7 will discuss how the emissivity for a particular paint sample is independent of wavelength, but dependent on angle of incidence. And thus, Equation (2-26) is further refined into the following:

$$M_e(T,\theta) = \varepsilon(\theta) \int_{\lambda_1}^{\lambda_2} \frac{2\pi hc^2}{\lambda^5 \left(e^{hc/\lambda kT}-1\right)} d\lambda \; .$$ (Eq 2-27)

2.2.5 Kirchoff's Law

Radiant energy incident on a surface in thermal equilibrium may undergo three processes: a portion of the energy may be absorbed, a portion may be reflected, and/or a portion may be transmitted. The ratios of these three portions of energy to the original incident energy are termed absorptance (α), reflectance (ρ), and transmittance (τ), respectively. The conservation of energy requires that the three fractions equal unity:

$$\alpha + \rho + \tau = 1, \qquad\qquad \text{(Eq 2-28)}$$

where

$$\alpha \equiv \frac{\Phi_{absorbed}}{\Phi_{incident}},$$

$$\rho \equiv \frac{\Phi_{reflected}}{\Phi_{incident}}, \qquad\qquad \text{(Eq 2-29)}$$

$$\tau \equiv \frac{\Phi_{transmitted}}{\Phi_{incident}}.$$

Kirchoff observed that, at a given temperature, the ratio of the exitance of a graybody to its absorptance was constant for all materials and equal to the exitance of a blackbody at the same temperature. This observation is known as Kirchoff's Law and can be stated as [9]:

$$\frac{M_e(\lambda, T)_{graybody}}{\alpha} = M_e(\lambda, T)_{blackbody}. \qquad\qquad \text{(Eq 2-30)}$$

From the discussion on emissivity, Equation (2-22) can be rearranged so that the exitance from a graybody is equal to the product of its emissivity and the exitance of a blackbody at the same temperature. Substituting into Equation (2-30) yields

$$\frac{\varepsilon \cdot M_e(\lambda,T)_{blackbody}}{\alpha} = M_e(\lambda,T)_{blackbody}.$$ (Eq 2-31)

Equation (2-31) implies that emissivity is equal to absorptance ($\varepsilon = \rho$), leading to the much recognized paraphrasing of Kirchoff's law as "a good absorber is a good emitter." Opaque materials, such as most aircraft surfaces, do not transmit energy ($\tau = 0$). Using Kirchoff's Law to replace absorptance with emissivity in Equation (2-28) for an opaque material yields

$$\varepsilon + \rho = 1.$$ (Eq 2-32)

This relationship allows the emissivity of a material to be determined from its reflectance, which is generally easier to measure [9].

2.3 A Large Commercial Aircraft

The faceted model was intended to be generic in nature but still based on a real aircraft. The aircraft chosen to model is the Boeing 747-400 four-engine passenger jet. The 747-400 depicted in Figure 2-5 served as the basis for the dimensions used in the creation of the various aircraft parts. The faceted model was meant to reflect the dimensions and configuration of the 747-400, not to exactly replicate it. Simple shapes were used to create the various parts of the aircraft as will be discussed in Chapter III. The main fuselage is represented by a cylinder, so the signature Boeing 747 hump (see Figure 2-5, side view) is not modeled. The dimensions were derived from the Boeing Commercial Aircraft Airport Planning Guide [1] whenever possible. Other measurements were obtained from a 1:100 scale plastic model manufactured by HobbyCraft of Canada. Default engine temperatures in the graphical user interface
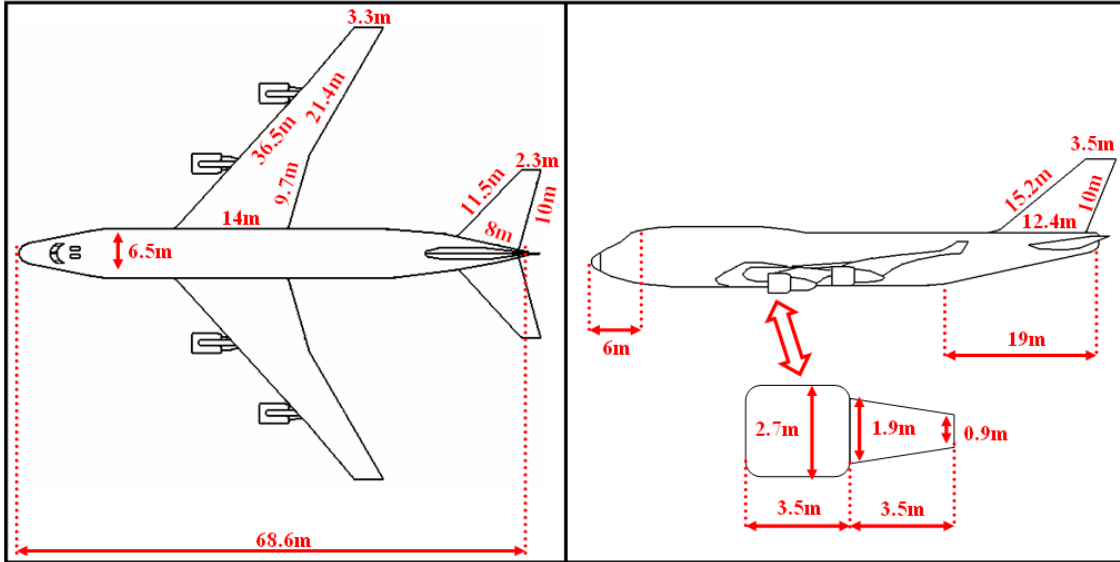
Figure 2-5: Key dimensions of the Boeing 747-400 used in creating the faceted model [1].

(GUI) are fictional to avoid sensitive results. However, the temperatures can be set by the GUI user to realistic values.

2.4 Summary

The fundamental radiometric concepts, specifically blackbody radiation and the relationship between emissivity and reflectance as defined by Kirchoff's Law, presented in this chapter will be key in the calculation of aircraft intensity in Chapter III. However, prior to any radiometric calculations, the faceted model must first be created based on the dimensions of the Boeing 747-400 discussed in the previous section.

III Radiometric Model

3.1 Overview

Although many computer-aided design programs could have been used to create the faceted model, MATLAB$^®$ was chosen so that knowledge gleaned from the creation of aircraft parts using facets could be applied to the obscuration and reflection algorithms. The obscuration algorithm and resultant matrix determines which facets contribute to the aircraft's intensity. The reflection matrix accounts for contributions from earth-shine, sky-shine, and part reflections to the aircraft's intensity. Surface properties for a specific paint sample are then derived from reflectance measurements. Atmospheric effects are discussed before concluding the chapter with the radiometric calculations necessary in determining the aircraft's intensity.

3.2 3-D Modeling in MATLAB$^®$

Before creating the radiometric model, a mathematical representation of the physical aircraft had to be created in MATLAB$^®$ using the dimensions discussed in Chapter II. To accomplish this, an understanding of how MATLAB$^®$ handles 3-D graphics was necessary. The *surf* command, used to display 3-D images, requires three square coordinate matrices (x, y, and z) to render an image [13]. Each x-coordinate element is matched with its corresponding y-coordinate and z-coordinate elements to create a single vertex on a rectangular grid. Each facet is created from four vertices, where vertices 1 and 2 are on one row and vertices 3 and 4 are on the row immediately below as depicted in Figure 3-1. For example, the first facet is created in the following fashion: First vertex 1 (x11,y11,z11) is plotted, then vertex 2 (x12,y12,z12), followed by vertex 3 (x22,y22,z22), and finally vertex 4 (x21,y21,z21) is plotted in-plane with the

$$\begin{pmatrix} x_{11} & x_{12} & x_{13} & x_{14} \\ x_{21} & x_{22} & x_{23} & x_{24} \\ x_{31} & x_{32} & x_{33} & x_{34} \\ x_{41} & x_{42} & x_{43} & x_{44} \end{pmatrix} \begin{pmatrix} y_{11} & y_{12} & y_{13} & y_{14} \\ y_{21} & y_{22} & y_{23} & y_{24} \\ y_{31} & y_{32} & y_{33} & y_{34} \\ y_{41} & y_{42} & y_{43} & y_{44} \end{pmatrix} \begin{pmatrix} z_{11} & z_{12} & z_{13} & z_{14} \\ z_{21} & z_{22} & z_{23} & z_{24} \\ z_{31} & z_{32} & z_{33} & z_{34} \\ z_{41} & z_{42} & z_{43} & z_{44} \end{pmatrix}$$
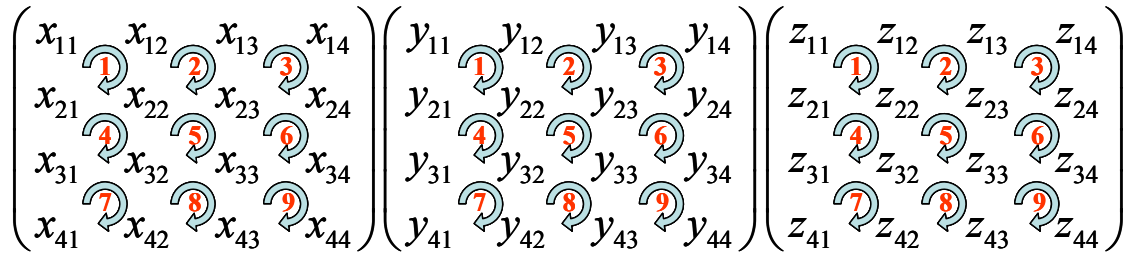
Figure 3-1: The coordinate matrices used to create facets necessary for 3-D modeling. Matrices are square (NxN) and create $(N-1)^2$ facets.

three other vertices. The resultant quadrilateral created by these four vertices becomes the first facet. Figure 3-2 shows the resultant facets from the matrices shown in Figure 3-1. The size of the matrices (NxN) determines the number of facets that will be generated $(N-1)^2$. More facets create better detailed parts, but also increase the time required in the radiometric computations. These issues will be discussed later.

3.3 Faceted Model

The next step is to take the knowledge of how MATLAB® creates faceted surfaces and use geometry to create the simple shapes which comprise the various aircraft
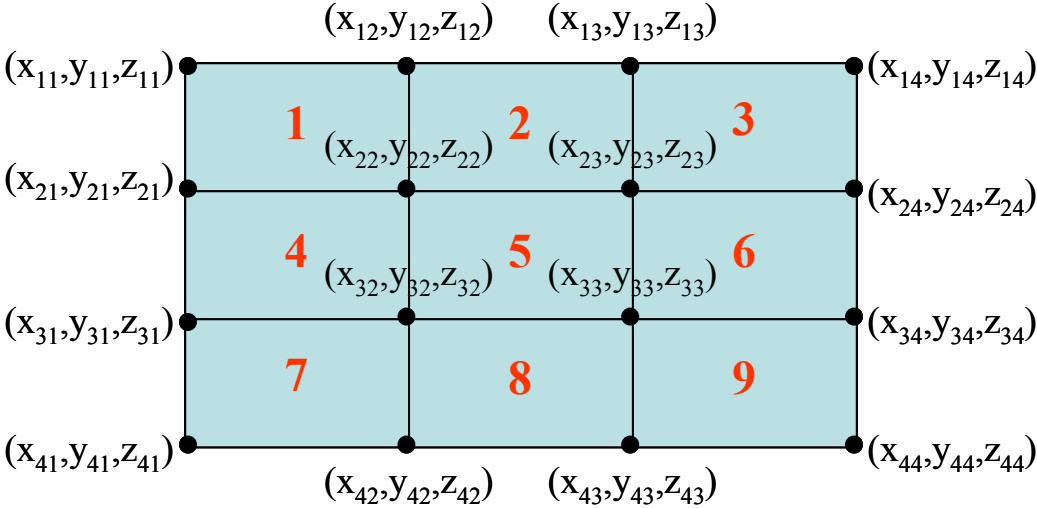
Figure 3-2: Nine facets and the vertices that created them.

parts. A complete aircraft parts breakdown is shown in Appendix C.

3.3.1 Fuselage

The fuselage is broken up into nine different parts as shown in Figure 3-3. The midsection of the fuselage is made of two half-cylinders whose coordinates are defined by [4]:

$$\begin{aligned}
x &= r\cos\theta, \\
y &= r\sin\theta, \\
z &= z.
\end{aligned}$$
(Eq 3-1)

In Equation 3-1, r is the radius of the cylinder and θ is varied from 0 to π in order to create half cylinders. Varying θ from 0 to 2π would create a full cylinder. The z-coordinate vector is varied from 0 to the length of the cylinder. Figure 3-4 shows the fuselage cylinder using the coordinate system and variables from Equation (3-1). The cylinder shown in Figure 3-4 is rotated and shifted into place using Euler's angles, which will be discussed later.
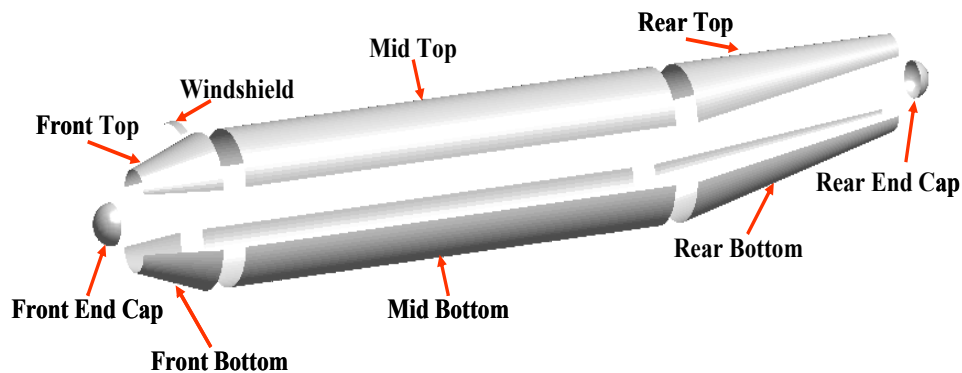
Figure 3-3: The fuselage is created from nine different parts. Different surface properties can be applied to each part to better simulate a real aircraft.
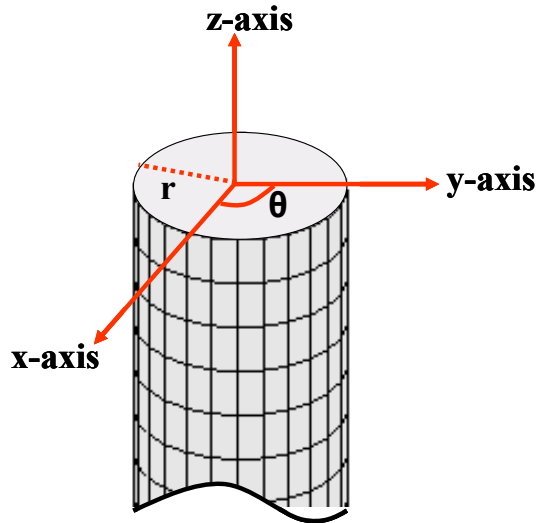
Figure 3-4:   The coordinate system and variables used to create the fuselage cylinder.   The cylinder is later rotated and shifted into place using Euler's angles.

The front and rear fuselage pieces are half-cones and are created much like regular cylinders; however, the radius is also varied. The rear fuselage pieces also incorporate a small offset (the difference between the start radius and the radius vector) in order to keep the top piece level with the mid fuselage and to give the bottom piece its slope.

The front and rear end caps are just hemispheres and can be created using the following [4]:

$$x = r \sin \theta \cos \phi,$$
$$y = r \sin \theta \sin \phi, \qquad\qquad \text{(Eq 3-2)}$$
$$z = r \cos \theta.$$

In order to create a hemisphere, the angles θ and ϕ are both varied from 0 to π.

3.3.2   Wings, Vertical Stabilizer, and Horizontal Stabilizers

The wings, vertical stabilizer, and horizontal stabilizers are created using trapezoids for the control surfaces themselves and half cones for the leading edges. The y-coordinate vector varies from 0 to the height of the trapezoid. The x-coordinate vector

varies from x_{start} to x_{end} which can be calculated from the well-known equation of a line [20]:

$$x_{start} = \frac{y - b_1}{m_1},$$

$$x_{end} = \frac{y - b_2}{m_2}.$$

(Eq 3-3)

Figure 3-5 shows the variables used in Equation 3-3 and also illustrates both parts of the wing/stabilzers. The slopes, m_1 and m_2 can be calculated using rise/run for each line. If the first y-intercept (b_1) is set to 0, the other (b_2) becomes $-m_2*$ *base length* (the longer of the two parallel lines). The z-coordinate vector is set to 0 for the first half of the matrix, then varies from 0 to the maximum radius of the leading edge cone for the wings and the horizontal stabilizers. This makes the bottom surface of the wing and horizontal stabilizers completely flat, while the top surface has a twist to it. The vertical stabilizer's z-coordinate vector varies from -1/2 the maximum radius of its leading edge to +1/2 the maximum radius of its leading edge to give it symmetry unlike the wings and horizontal stabilizers.
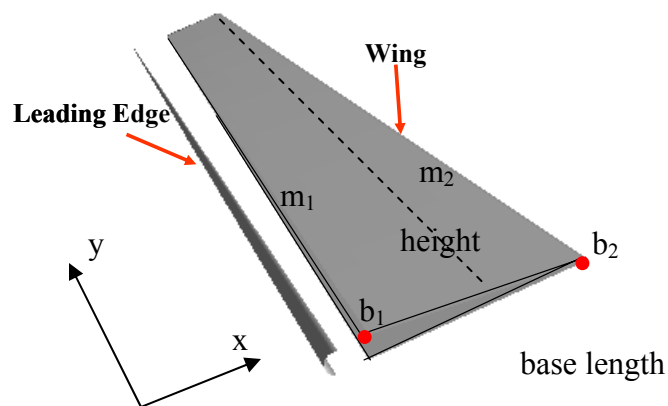
Figure 3-5: The wings and stabilizers are created from trapezoids and half-cone leading edges.

3.3.3 Engines

The engine is assembled from seven simple shapes as portrayed in Figure 3-6. The case top and bottom are created in the same manner as the mid fuselage top and bottom already discussed. The exhaust cone has its analog in the front fuselage cone. The front face, interface washer, and exhaust plane are all simply disks created using Equation (3-1). The difference in the equation is that the radius is varied from 0 to the disk radius for both the front face and exhaust plane and from an inner radius to outer radius for the interface washer. The angle θ is varied from 0 to 2π and the z-coordinate vector is not varied at all.

3.3.4 Rotation and Translation

All aircraft parts were created centered on the origin then rotated and moved to their final positions. The rotation and translation of one point, (x_1, y_1, z_1), to another, (x_2, y_2, z_2), is given by Equation 3-4 [7].
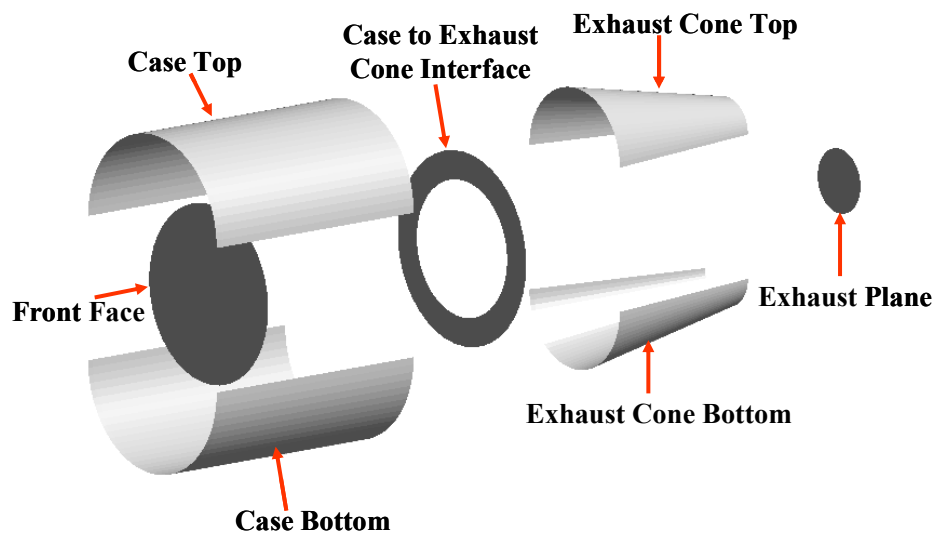
Figure 3-6: Each engine is constructed from seven parts. Each part can be assigned its own temperature and surface properties.

$$x_2 = L_x + a_{11}x_1 + a_{12}y_1 + a_{13}z_1$$
$$y_2 = L_y + a_{21}x_1 + a_{22}y_1 + a_{23}z_1 \qquad \text{(Eq 3-4)}$$
$$z_2 = L_x + a_{31}x_1 + a_{32}y_1 + a_{33}z_1$$

Where L_x, L_y, and L_z are the components of the translation and a_{ij} are elements of

$$a = \begin{pmatrix} \cos\psi\cos\chi & -\cos\psi\sin\chi & \sin\psi \\ \cos\phi\sin\chi + \sin\phi\sin\psi\cos\chi & \cos\phi\cos\chi - \sin\phi\sin\psi\sin\chi & -\sin\phi\cos\psi \\ \sin\phi\sin\chi - \cos\phi\sin\psi\cos\chi & \sin\phi\cos\chi + \cos\phi\sin\psi\sin\chi & \cos\phi\cos\psi \end{pmatrix}. \text{(Eq 3-5)}$$

The angles φ, ψ, and χ are known as the Euler angles and control rotation about the origin as follows: φ about the x-axis, ψ about the y-axis, and χ about the z-axis. In general, (x_1, y_1, z_1) can be scalars, vectors, or matrices.

3.3.5 Facet Normals and Areas

Each facet must be assigned a normal to its surface and an area to be used in the projected area analysis and other computations. To find these, each facet is broken down into four vectors emanating from two opposite vertices as shown in Figure 3-7. These vectors are $\overrightarrow{BA}$, $\overrightarrow{BC}$, $\overrightarrow{DC}$, and $\overrightarrow{DA}$. Taking the cross product of $\overrightarrow{BA}$ and $\overrightarrow{BC}$ or $\overrightarrow{DC}$ and $\overrightarrow{DA}$ will result in a vector perpendicular to the facet surface, i.e., its normal [4]. The right-hand rule dictates which way the normal will point. $\overrightarrow{BA} \times \overrightarrow{BC}$ will result in the
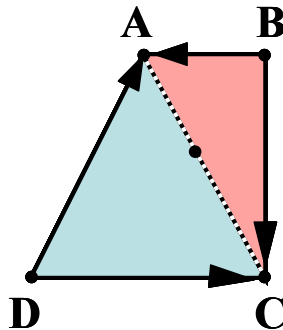
Figure 3-7: Each facet can be broken up into four vectors which can be used to calculate the facet normal and facet area.

normal pointing out of the page, while $\overrightarrow{BC} \times \overrightarrow{BA}$ will result in a normal pointing into the page. The cross product can be found by the following:

$$\vec{F} \times \vec{G} = (F_y G_z - F_z G_y)\hat{x} + (F_z G_x - F_x G_z)\hat{y} + (F_x G_y - F_y G_x)\hat{z} .\qquad \text{(Eq 3-6)}$$

When creating parts, it is imperative that the normals are directed *outward* from the surface of interest. Figure 3-8 shows two equivalent parts with opposite normals. Both hemispheres are exact in dimensions, but significant differences would occur in the projected area calculations. Plotting the normals is the only way to know whether the part was generated correctly. From Equation (3-2), θ is varied from 0 to π to create the hemisphere on the left in Figure 3-8 and from π to 0 for the hemisphere on the right – a very subtle difference that would have drastic consequences. Figure 3-9 shows that the aircraft facet normals are oriented outwards as expected. In MATLAB®, this figure can be rotated to view all facet normals.

A   **B**
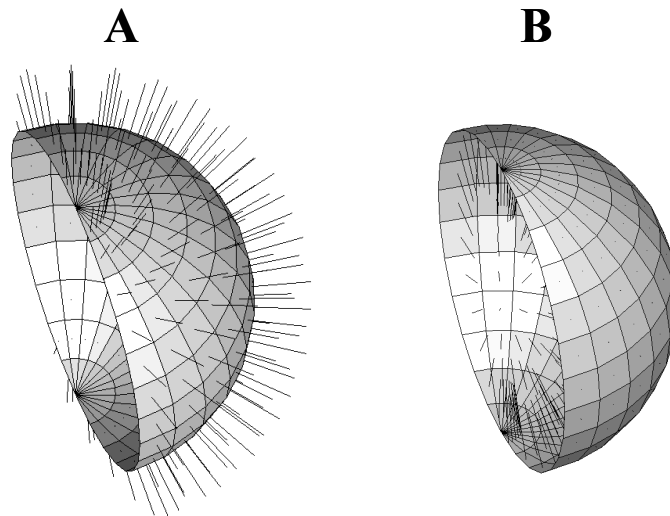
Figure 3-8: The two hemispheres are exact in dimensions; however, the normals for **A** are directed *outward*, while those for **B** are directed *inward*. Plotting the normals is the only way to know that these hemispheres are different. Not checking the normals could lead to incorrect calculations.
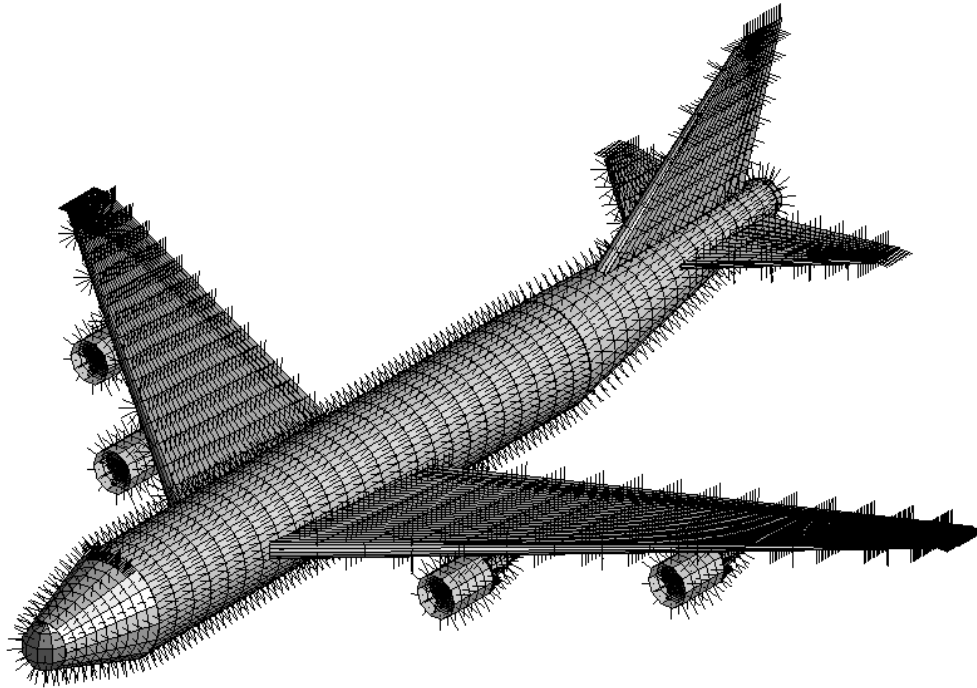
Figure 3-9: The aircraft facet normals. Notice the normals are pointing out from the aircraft facets.

Half the magnitude of the cross product of two vectors, $\frac{1}{2}\left|\vec{F}\times\vec{G}\right|$, yields the area of

a triangle whose sides are $\vec{F}$, $\vec{G}$, and the line connecting $\vec{F}$ and $\vec{G}$ [20]. Therefore,

$\frac{1}{2}\left|\overrightarrow{BA}\times\overrightarrow{BC}\right|$ results in the area of the triangle created by A, B, and C as shown in Figure

3-7.   Similarly, $\frac{1}{2}\left|\overrightarrow{DC}\times\overrightarrow{DA}\right|$ yields the area of the triangle created by C, D, and A.

Summing the areas of these two triangles results in the total area of the facet as shown in

Figure 3-7.   Recall from Chapter II that if the area of the source and detector are much

smaller than the distance between them squared ($A_s, A_d << R^2$), the intensity from the

source is simply the product of the projected area ($A_s \cos \theta_s$) and radiance of the source

(Equation (2-13)). As a result of this section, the projected area can be computed for

each facet based on its area, A_s, and the angle, θ_s, between the observation line and the facet's assigned normal[7].

3.4   Facet Area Errors

Using flat facets to create surfaces involves some obvious errors, especially when creating curved surfaces such as cylinders, disks, and spheres. To minimize errors, a large number of small facets should be used (i.e., high resolution). High resolutions have the unfortunate side-effect of increasing computation times in the obscuration algorithm, reflection algorithm, and radiometric calculations. The effects on the obscuration and reflection algorithms are especially significant. Through trial and error, resolutions were selected for each part based on the faceted appearance of the part and the overall effect on computational times in the creation of the obscuration and reflection matrices. Table 3-1 outlines the geometric area of parts along with the area summed from the facets that create the part. The amount of error is based on the ratio of the facetized part to the geometric area of the part and is listed in the table. As expected, flat surfaces such as the wings, vertical stabilizer, and horizontal stabilizers have no error. The main fuselage (mid, front, rear) has relatively little error due to the higher resolution used to create these parts. The hemispherical caps, on the other hand, have about an 8% error in area, but only represent 0.86% of the total aircraft surface.

The largest errors occur in the creation of disks such as the engine front, engine to exhaust cone interface (washer), and exhaust disk.

---

[7] To find the angle between the observer and normal, $\overrightarrow{Obs}$ and $\widehat{n}_s$: $\theta_s = \cos^{-1}\left(\dfrac{\overrightarrow{Obs} \cdot \widehat{n}_s}{\left| \overrightarrow{Obs} \right| \left| \widehat{n}_s \right|} \right)$ [20].

Table 3-1: Errors in surface area as a result of representing that surface using facets.

Aircraft Part	Geometric Area (m²)	Faceted Area (m²)	Error	# of Facets
Mid Fuselage	778.02	777.50	6.68×10^{-4}	1250
Front Fuselage	92.33	91.76	0.0062	162
Rear Fuselage	272.69	270.31	0.0087	450
Front Fuselage Cap	13.03	11.98	0.081	25
Rear Fuselage Cap	9.82	9.03	0.080	25
Wing	482.67	482.67	0	841
Vertical Stabilizer	151.05	151.05	0	289
Horizontal Stab	83.43	83.43	0	169
Engine Case	29.69	29.20	0.017	50
Engine Front	4.91	4.25	0.13	81
Engine Washer	2.89	2.53	0.12	81
Exhaust Cone	12.08	11.86	0.018	50
Exhaust Disk	0.64	0.55	0.14	81

The obvious choice is to increase the resolution to correct these errors. Figure 3-10 is an error analysis tool to help determine what resolution to use in creating a disk or washer. This tool works for the engine front face, exhaust disk, and interface washer. For an error of less than 1%, at least 676 facets (resolution of 27) must be used in the creation of the part.

Of course changing the resolution of these parts would also require the generation of new obscuration and reflections matrices. An alternative is to add a correction to the desired temperature or to the area of the part. Since the engine front face is cool and does not contribute significantly to the overall intensity of the aircraft, the correction only needs to be applied to the interface washer and exhaust disk.

First, an assumption must be made that the self emission of the part must be much greater than any reflection off its surface. This certainly applies for hot parts such as the
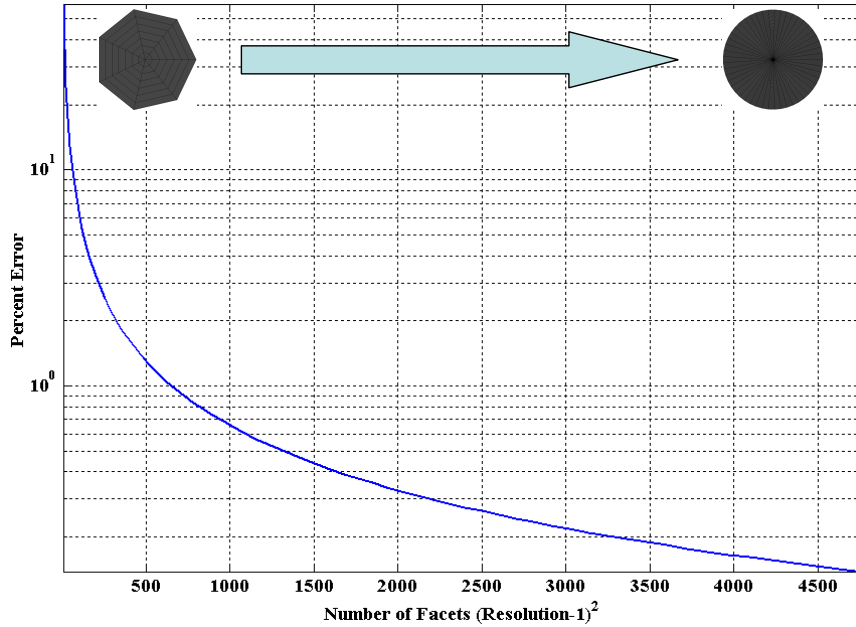
Figure 3-10: The amount of error as a function of the number of facets used to create a circular disk or washer. Note that for an error of less than 1%, at least 676 facets (resolution of 27) are needed.

interface washer and exhaust disk. Intensity can then be approximated as the product of the projected area and part radiance as previously shown in Chapter II.

$$I_e \cong \frac{\Phi_e}{\Omega_d} \cong L_e A_s \cos\theta_s .$$
(Eq 3-7)

Since the faceted area is less than the real area, then an increase in the facet's area by the same fraction will correct the intensity. Scaling the area is preferred since it only requires a small change in the code. However for the current code, an increase in the radiance by the same fraction as the area error must be used. Note that radiance is a function of both the temperature and wavelength and in order to find a correction factor, the radiance must first be solved for at a specific temperature. The facet error is then added to the radiance and the corrected temperature is back-solved from the corrected radiance. The ratio of the corrected temperature to the original temperature yields a

corrective scaling factor. The process just described was repeated for a range of temperatures (200-1000 K) and range of errors (1%-15%) to develop Figure 3-11. Using MATLAB® curve fitting yields

$$\text{scale factor}_{\text{LWIR}} = 8.0075 \times 10^{-5} x^2 + 3.0487 \times 10^{-3} x + 1.0024, \qquad \text{(Eq 3-8)}$$

$$\text{scale factor}_{\text{MWIR}} = 2.7963 \times 10^{-4} x^2 + 5.199 \times 10^{-5} x + 1.0125, \qquad \text{(Eq 3-9)}$$

where x is the **percent** error.

For example: the desired temperature for the exhaust disk is 700 K, the exhaust disk has a 14% error in area, and the band of interest is LWIR. Using Equation (3-13), a scale factor of 1.06 is calculated. Therefore, the corrective temperature to enter into the radiometric model is 742 K.

Figure 3-11: Temperature correction plots to compensate for error in facet area. Self emission from the part must be much greater than any reflections off that part.
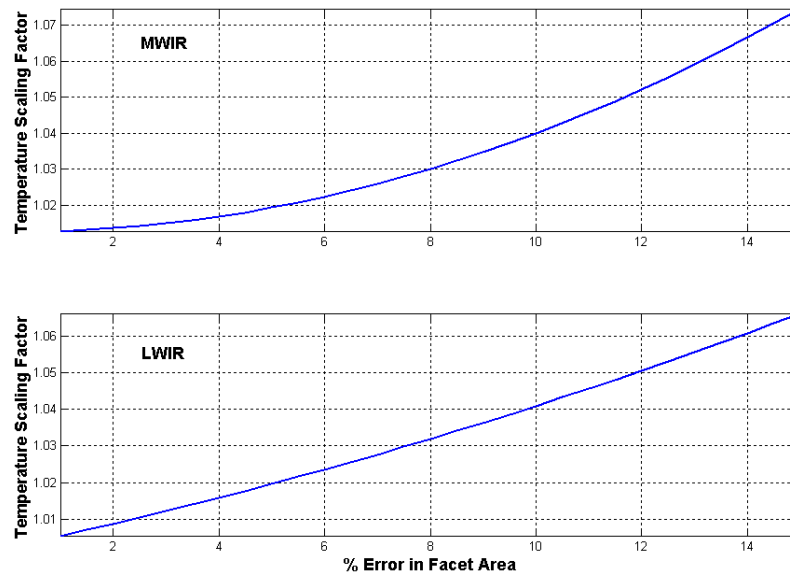
3.5   Obscuration Matrix

3.5.1   The Obscuration Algorithm

The only facets that contribute to the overall intensity of the aircraft are those that are visible to the observer. Those facets whose normals are greater than 90º from the observer are obviously not in view and are easy to account for; however, there are facets whose normals are not greater than 90º from the observer, but are still obstructed by another facet and thus do not contribute to the overall intensity. These obstructed facets are not as easy to account for. Each facet needs to be checked with every other facet in order to determine if it obstructs other facets or is obstructed by other facets. This is a very computationally intensive process to be done during a simulation. Therefore, obscuration matrices were developed for several aircraft pitch angles. These matrices are accessed during radiometric calculations allowing the simulation to run in a much shorter time. Each matrix determines which facets are in view and which are obstructed for 0-360º in azimuth. Each matrix takes about three hours to construct using MATLAB$^®$ 7 and about six hours using MATLAB$^®$ 6. Once constructed, the matrices do not need to be reconstructed unless resolutions are changed or new parts are added.

Figure 3-12 illustrates how the algorithm determines whether or not one facet obscures another. The distance projected from the center of facet B onto the observation line, $\overrightarrow{Obs}$, is given by Equation (3-10) [20].

$$\text{distance} = \overrightarrow{AB}\sin\theta = \frac{\left|\overrightarrow{AB}\times\overrightarrow{Obs}\right|}{\left|\overrightarrow{Obs}\right|} \qquad\qquad \text{(Eq 3-10)}$$
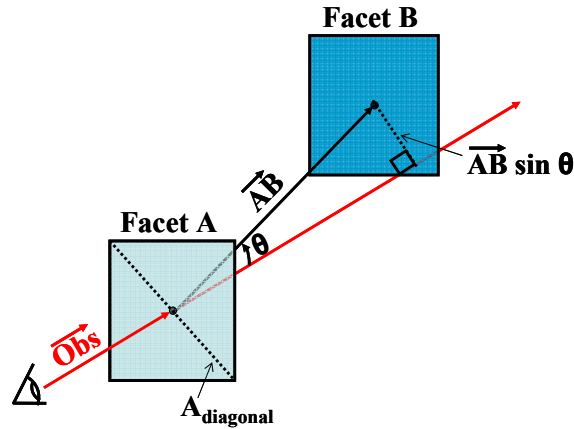
Figure 3-12: The obscuration of facet B by facet A is determined by the projected distance from facet B's center onto the observation line.   This distance is compared to the projected diagonal of facet A. If the distance is less than the projected diagonal, then facet A obscures facet B as in the figure above.

This distance is then compared to the projected diagonal[8] of facet A. If the distance is less than half the projected diagonal, then the first facet obscures the second. Otherwise, there is no obscuration. For efficiency, obscuration is checked both ways for each look angle. First, obscuration of facet B by facet A is checked; then obscuration of facet A by facet B is checked. The direction of $\overrightarrow{AB}$ allows the algorithm to determine which facet is in front (closer to the observer).

Figure 3-13 shows the obscuration matrix at work. In the top figure, the observer is directly viewing the broadside of the aircraft. In the bottom figure, the whole scene, including the observer, is slightly rotated to show the facets that are not in view by the observer. These facets are darker than the surrounding facets and look like "shadows". The two engines cast a shadow on the fuselage, while the two opposite engines are entirely in the shadow of the fuselage.

---

[8] The length of the diagonal is multiplied by the cosine of the angle between the facet normal and the observation line. As the angle approaches 90º, the facet becomes less visible and the cosine of the angle approaches zero.
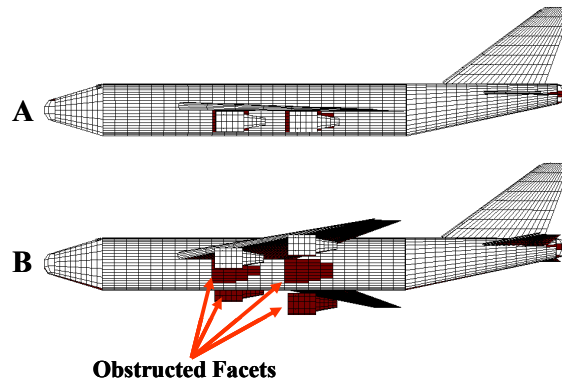
Obstructed Facets

Figure 3-13: The obscuration matrix at work. The observer is viewing the broadside in **A**. In **B**, the observer is still viewing the broadside, but the whole scene, including the observer, have been slightly rotated to show the "shadow" cast by the obscuration matrix. The "shadowed" facets cannot be seen by the observer as is evidenced in **A**.

3.5.2   Obscuration Errors

Figure 3-13 is a good example of when the obscuration matrix is working well. However, there are instances when facets are incorrectly obscured or not obscured when they should be. Figure 3-14 illustrates both of these examples. The graphic on the left illustrates a situation when a facet should be obstructed by the algorithm, but is not. The observer is looking into the page and so the distance from the center of the second facet to the observation line is greater than half the *projected* diagonal of the first facet. The algorithm would incorrectly conclude that the second facet is not obscured by the first, even though it is obviously obstructed. The graphic on the right is an example of the algorithm obscuring a facet when it should not be. Again, the observer is looking into the page, but in this case the distance from the second facet center to the observation line is less than half of the projected diagonal length due to a large first facet diagonal. The algorithm would obscure the second (darker) facet even though it is not being obscured.
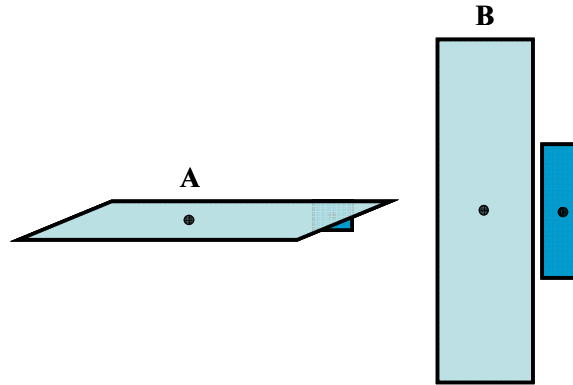
Figure 3-14: Instances where the obscuration matrix fails. In **A**, the light colored facet should obscure the smaller one in the upper right hand corner. However, due to the projected diagonal length, the algorithm may not obscure the smaller facet. In **B**, due to the size of the diagonal of the lighter facet, the algorithm will obscure the darker facet even though it is obviously not obscure.

The ideal scenario is to have equally-sized and many (high resolution) facets on all the aircraft parts. For this model, the resolution on each part was adjusted to get similar facet densities. However, due to geometric differences in parts (singly curved, doubly curved, flat, etc.) the facet shapes are not necessarily the same. Most of the facets are quadrilateral but not necessarily the same shape (square, rectangular, trapezoidal, etc.). There are a few facets primarily on the hemispheres that are triangular. The location of these triangular facets at the front and rear of the aircraft keep them from obscuring or being obscured and thus do not present a problem.

To determine whether these obscuration errors are significant, the obscuration matrix was tested for an aircraft elevation angle of -20º. All the surface temperatures were set to 295 K and emissivity for every facet was set to one. With no reflection contributions and no temperature contrast between parts, the effects of the obscuration matrix can be examined as shown in Figure 3-15 and already seen in Figure 3-13. In Figure 3-15, the aircraft on the left is at an azimuth angle of 45º and represents the
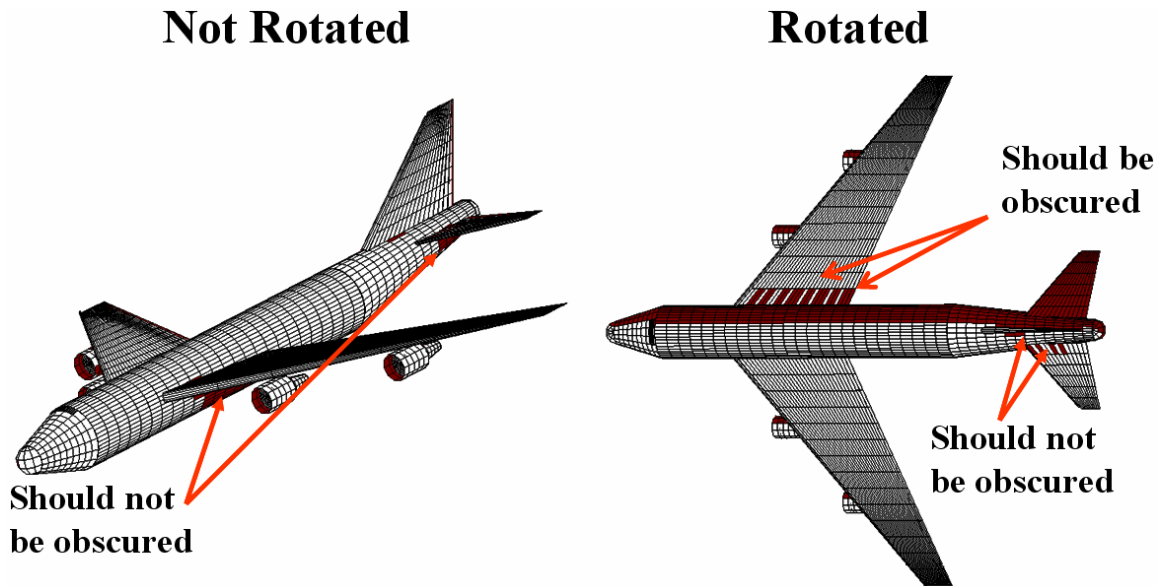
Not Rotated   **Rotated**

Figure 3-15: Obscuration errors on an aircraft at -20º elevation and 45º azimuth (not rotated).

aircraft as viewed by the observer. As shown in this image, there are several facets on the fuselage under the wing and horizontal stabilizer that are obscured, but should not be. In the same image, only the outer surface of the front engine cavity is modeled, explaining why the inner surface 'looks' obscured – these can be ignored. The figure on the right is rotated to see the facets not viewable to the observer. There are several facets on the left wing, including a whole row of them, which should be obscured by the fuselage but are not. There are also four facets on the right horizontal stabilizer that are obscured but should not be.

To view what effect these obscuration errors have, the major aircraft component intensities are plotted in Figure 3-16 using the same aircraft temperatures and surface properties discussed above. The obscuration matrix works well at nose-on, tail-on, and broadside views as demonstrated in Figure 3-13 for the broadside view. These aircraft aspect angles (0º, 360º, 90º, 270º) serve as minimal error points. As can be seen from
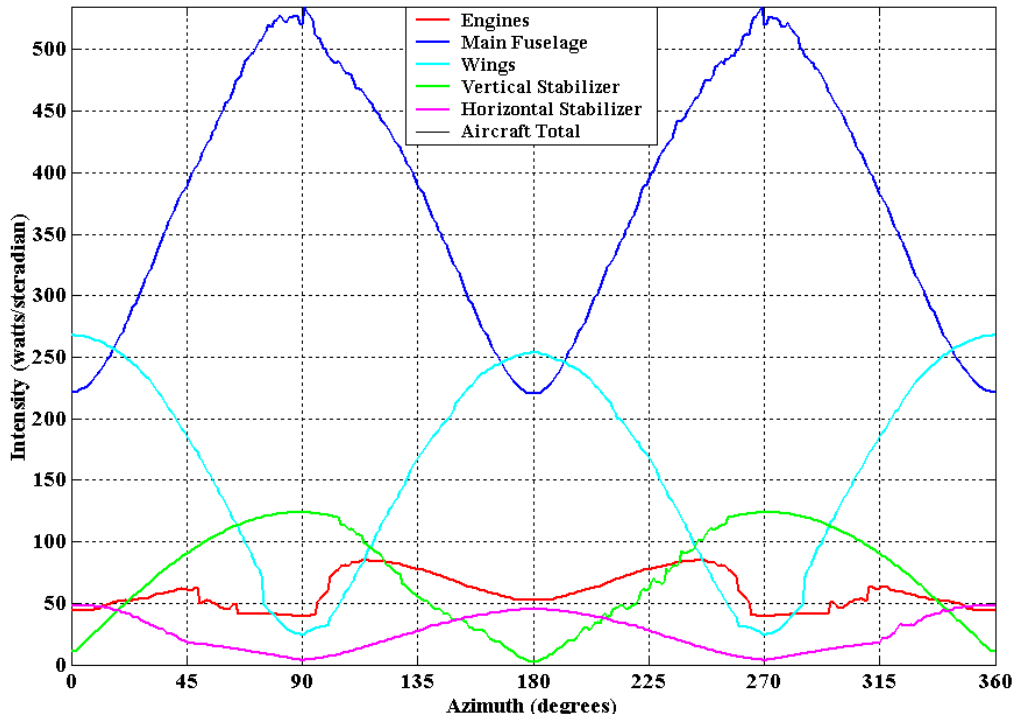
Figure 3-16: The major aircraft component intensities when configured for obscuration matrix effects at -20º elevation. The obscuration errors contribute to the jaggedness seen in some of the signatures, but do not affect the trend of the signatures.

Figure 3-16, all aircraft part intensities transition from and to these low error points with little deviation. The only exception is the intensity due to the engines, which has notches between 46º and 105º and again between 255º and 315º. These notches occur when two of the engines become completely obscured by the fuselage and are actually examples of the obscuration matrix working well.

While hard to quantify, the errors due to obscuration create some 'jaggedness' to the aircraft component signatures, but do not adversely affect the trend of these signatures. Since the goal is to develop a trend analysis tool, the obscuration errors do not have a significant effect.

3.6   Reflection Matrix

3.6.1   *Reflection Algorithm*

The radiometric model also features a single bounce reflection[9] matrix to account for single reflections of hot parts, as well as earth shine and sky shine. The algorithm starts by tracing a single ray from the observer to a facet in view. Using Snell's law, this ray reflects off the facet at the same angle[10] as the incident angle, labeled θ_i in Figure 3-17. The ray is then followed to see whether it strikes another facet, earth, or sky. The same procedure used in the obscuration matrix is implemented to check whether the ray intersects another facet. In Equation (3-10), the observer line, $\overrightarrow{Obs}$, is replaced with the reflected ray, but all else remains the same. If the distance from the center of the second facet to the reflected ray is less than half the projected diagonal of the first facet,

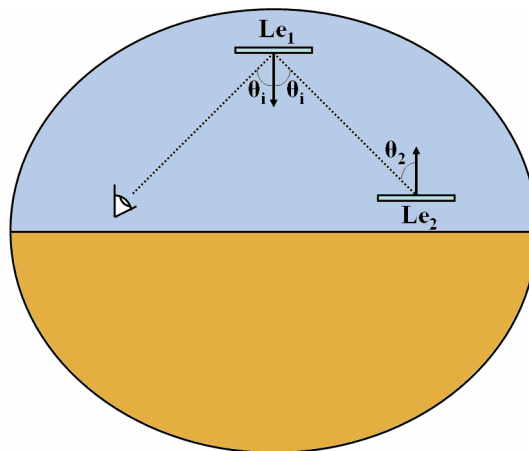Figure 3-17: The reflection algorithm traces a single ray reflected off a facet according to Snell's Law and then checks whether the reflected ray strikes another facet, the earth (lower hemisphere), or the sky (upper hemisphere). The radiance from another facet, earth, or sky is then reflected off the first facet.

---

[9] The algorithm assumes a fairly specular surface (Section 3.7 will show this to be a good approximation).

then the ray is said to strike the second facet. Of course, the second facet must be in view of the first and so the magnitude of θ_2, shown in Figure 3-17 must be less than 90º.

Figure 3-18 is an example of the reflection matrix at work. All aircraft parts are set to the same temperature (295 K) except for the leading edge of the vertical stabilizer. This part is set to a higher temperature (500 K). The emissivities of the parts are all set to 0.2, making the reflectances 0.8. Also, the parts are assumed to be purely specular (more will be discussed in Section 3.7). This configuration allows the reflection to have some contrast. The reflection of the hot leading edge on the fuselage can be distinctively seen in Figure 3-18. Since the emissivity of the heated surface is only 0.2 and the reflectance of the fuselage is 0.8, only a portion of the radiance from the heated surface reflects off the fuselage. This accounts for the difference in color (and thus radiance) between the heated leading edge and the reflection.
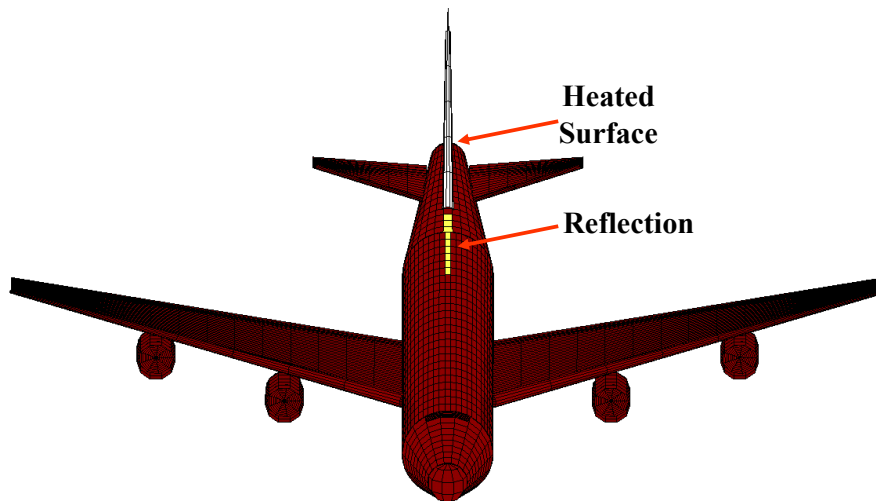

Figure 3-18: The reflection matrix at work. All aircraft parts are set to the same temperature except for the vertical stabilizer leading edge. The reflection of this heated part can be seen on the top portion of the fuselage.

---

[10] The angle is measured with respect to the facet normal.

If the reflected ray does not strike another facet, then it must strike either the earth or the sky. The resulting reflections are seen as either earth shine or sky shine. Both the earth and sky are assumed to have emissivities of 1.0. The amount of earth or sky shine seen is highly dependent on the true pitch and observed pitch of the aircraft. The true pitch of the aircraft is the angle made between the aircraft waterline and the horizon. Observed pitch is the apparent pitch seen by the observer. In Figure 3-19, both aircraft have an observed pitch of 0º, but the true pitches are different. The aircraft in **A** has a true pitch of 0º and as a result, the amount of earth and sky shine is roughly equal. The aircraft in **B** has a true pitch of 30º. Given an observed pitch of 0º, this implies that the observer is located at a higher altitude than the aircraft and thus a greater amount of sky shine is observed. The assumption is that an observer higher in altitude than the aircraft
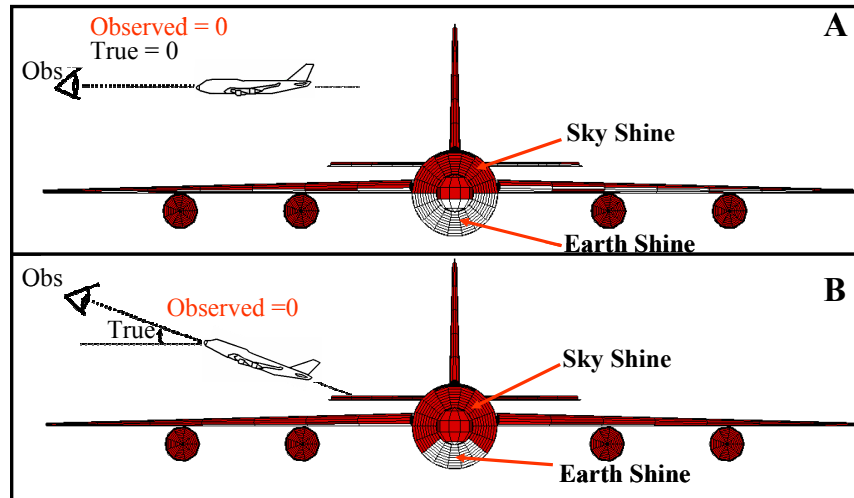
Figure 3-19: The reflection matrix showing earth and sky shine off the aircraft. Pitch angle (observed versus true) makes a difference in the amount of earth or sky shine. in **A**, the true pitch of the aircraft is 0º and the observed pitch of the aircraft is also 0º. in **B**, the true pitch of the aircraft is 30º, but the observed pitch is still 0º. This implies that the observer is above the aircraft. As a result, sky shine is prevalent on the aircraft.

will have the sky behind him, while one lower in altitude than the aircraft will have the earth behind him. This may not always be the case. For example, an observer on a mountain looking down on an aircraft in a valley will have the mountain, not the sky, behind him. If the observer is only slightly lower in altitude than the aircraft, the observer may have the sky behind him rather than the earth.

3.6.2   Reflection Errors

There are instances where the reflection algorithm may fail. Figure 3-20 illustrates such a case. The algorithm first checks if facet 2 reflects off facet 1. Since the normal of facet 2 is greater than 90º with respect to the reflected ray, facet 2 is not reflected off facet 1. The next step for the algorithm is to check if facet 3 reflects off facet 1. The algorithm does not account for the fact that facet 2 happens to be obstructing facet 3 and thus incorrectly reflects facet 3 off of facet 1. Although every reflection from every part at each elevation and azimuth angle has not been inspected, the errors described above appear on occasion when the observed pitch of the aircraft is greater than +15º. At these higher pitch angles, hot engine parts may reflect off the main fuselage even though the wing is obscuring the engines from the part of the fuselage the
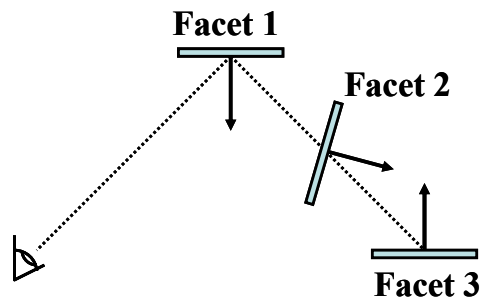
Figure 3-20: An example of when the reflection algorithm fails. The algorithm does not check for obstruction by another facet and would therefore incorrectly reflect facet 3 off of facet 1.

3-23

reflections are on. Inspecting the reflections off the faceted model, as in Figure 3-18, one can determine whether or not a reflection is valid. Section 4.9 will describe a procedure to check reflections.

3.7   Surface Properties

The radiometric model can use simple surface properties or a surface property matrix created from measured data. For simple surfaces, emissivity and reflectance are assumed to be angle and wavelength independent. However, real surfaces are rarely independent of angle and wavelength.

3.7.1   Paint Selection

Originally, the computational model was to be validated against the plastic, 1:100 scale, HobbyCraft model mentioned in Section 2.3 and depicted in Figure 3-21. The plastic model is not plumbed and therefore cannot be heated. In order to maintain its temperature, the plastic model fuselage was stuffed with insulating foam. It was originally painted with Krylon[®] 1602 ultra flat black paint for its high emissivity. However, flat black paint is not very specular and would thus invalidate the assumption of specularity used for the reflection algorithm. Discussions with personnel from the AFRL Optical Measurement Facility (OMF) confirmed that aircraft paints are generally specular at LWIR, but not necessarily so at MWIR [5]. At MWIR, aircraft paints still

Figure 3-21:   The plastic, 1:100 scale model manufactured by HobbyCraft of Canada. It is painted with an ultra flat black primer and a gloss black topcoat.

have a large specular contribution, but may have a significant diffuse component. This diffuse component is addressed in the radiometric calculations allowing for the assumption that the paint is still fairly specular. Airliners that do not paint their aircraft, but rather opt for the polished aluminum look, are very specular at both IR bands. In order to keep the specular assumption at both bands, the OMF suggested using gloss black paint. This paint is specular at both IR bands with high emissivity and a low diffuse reflectance. Therefore, the plastic model was painted with Krylon[®] 1601, glossy black, over the previous flat black paint. Figure 3-21 shows the painted plastic model.

3.7.2 *Hemispherical Diffuse Reflectance (HDR) Measurements*

A plastic sample with the flat black undercoat and glossy black top coat was provided to the OMF for a hemispherical diffuse reflectance (HDR) measurement. The HDR measurement provides the reflectance (total, diffuse, and specular components) as a function of wavelength for various incident angles. Figure 3-22 shows the specular component reflectance for both the MWIR and LWIR bands at 10º, 20º, 30º, 40º, 50º, 60º, 70º, 75º, and 80º angles of incidence. Note that the reflectance of the sample increases with increasing angle of incidence. The reflectances at each angle of incidence for both bands are fairly constant with respect to wavelength, which allows for a simplification. The reflectance is averaged for each incident angle and plotted as a single point on a reflectance versus incident angle graph as shown in Figure 3-23. An additional data point corresponding to a reflectance of 1.0 at 90º is added since at grazing, a reflection of 1.0 would be expected. The plotted data points are then used to find the reflectance as a function of incident angle for each band.
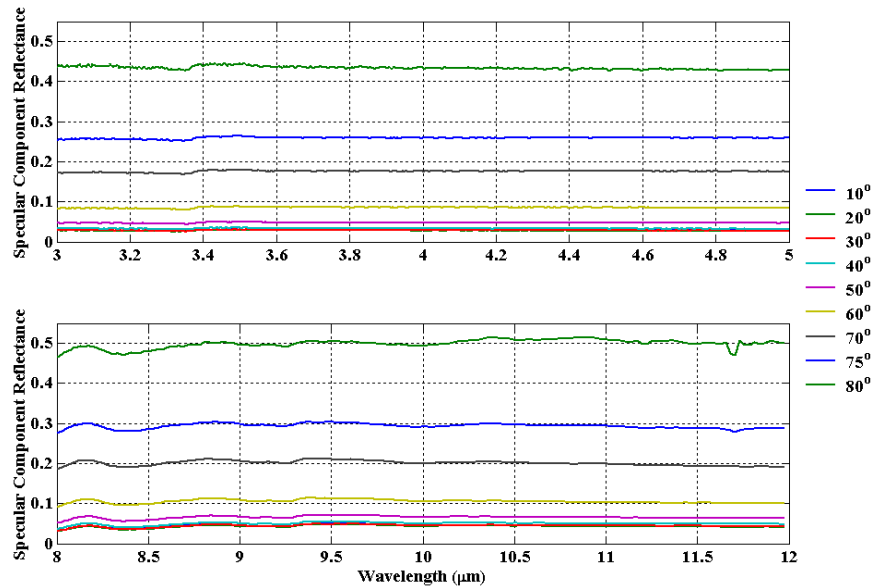
Figure 3-22: Hemispherical diffuse reflection (HDR) measurement taken by AFRL's Optical Measurements Facility of a plastic sample with a Krylon® 1602, ultra flat black, undercoat and a Krylon® 1601, glossy black, topcoat. There is little variance in reflectance over each infrared band, but significant difference in reflectance over different incident angles.
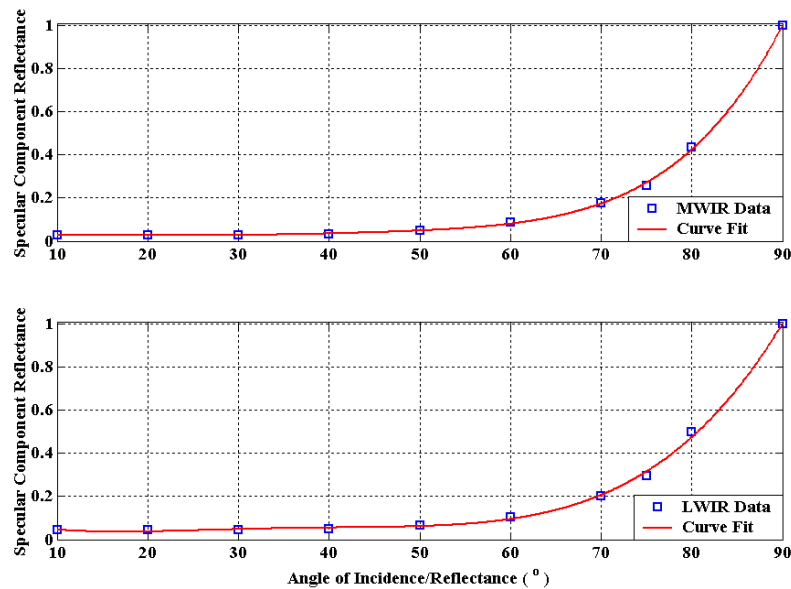

Figure 3-23: Since there is little variance in reflectance over each infrared band, an average reflectance is computed for each incident angle. The data is plotted and an equation is derived using the MATLAB® data fit tool. The resultant equation provides reflectance as a function of incident angle.

The MATLAB® data fit tool was used to find Equations (3-11) and (3-12) for MWIR and LWIR reflectances, respectively.

$$\rho_{MWIR}(\theta)=1.638\times10^{-9}\theta^5 - 2.756\times10^{-7}\theta^4 + 1.7974\times10^{-5}\theta^3$$
$$- 5.324\times10^{-4}\theta^2 + 6.918\times10^{-3}\theta - 2.720\times10^{-3}$$

(Eq 3-11)

$$\rho_{LWIR}(\theta)=1.040\times10^{-7}\theta^4 - 1.415\times10^{-5}\theta^3 + 6.848\times10^{-4}\theta^2$$
$$- 1.305\times10^{-2}\theta + 0.1206$$

(Eq 3-12)

The angle, θ, is the incident angle and, by Snell's Law [8], the reflected angle, as well. Figure 3-24 illustrates the use of Equation (3-11) as the reflectance function for the faceted model. As expected (recall Figure 3-23), the reflectance at angles closer to grazing (90º) is much higher than the reflectance at lesser incident angles. At the aspect angle shown, earth and sky shine are the main contributors to the reflected energy. For illustrative purposes, both earth and sky temperatures were set the same to show the effects of the reflectance function at MWIR.
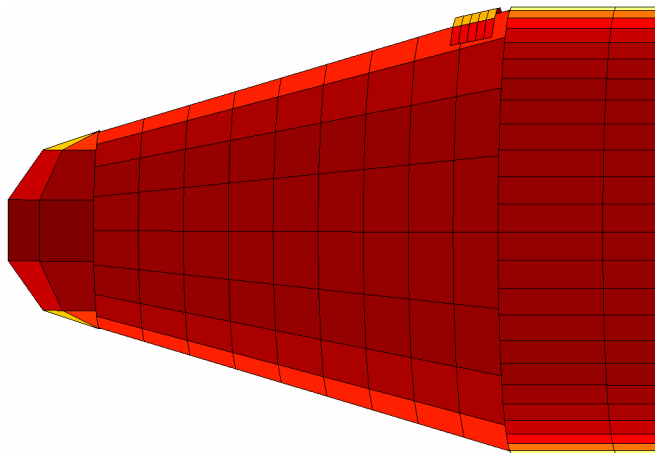

Figure 3-24: Zoomed in image of faceted aircraft nose. The angular dependence of the glossy black paint is shown. At angles near grazing (90º), reflectance is high, while at lesser angles reflectance is low. Note: earth and sky shine are the main contributors in this figure and are set to the same temperature at MWIR.

Using Kirchoff's Law, the angle-dependent emissivity can be determined by subtracting Equations (3-11) and (3-12) from 1.

$$\varepsilon_{M/LWIR}(\theta) = 1 - \rho_{M/LWIR}(\theta). \qquad \text{(Eq 3-13)}$$

Equations (3-11) through (3-13) are used later in the radiometric calculations.

Using the HDR data for the diffuse component reflectance, averaging the reflectance for each incident angle as was done for the specular component, and then using the MATLAB® curve fit tool yields the diffuse reflectance as function of incident angle as depicted in Figure 3-25. Since the diffuse component reflectance is so low for both bands, averaged reflectances of 0.0127 for MWIR and 0.0377 for LWIR are used later in the radiometric calculations.

3.7.3   Bi-Directional Reflectance Distribution Function (BRDF) Measurements

The HDR data proved useful in determining the angle-dependent reflectance of the paint scheme used on the plastic model aircraft, but led to questions about the specularity
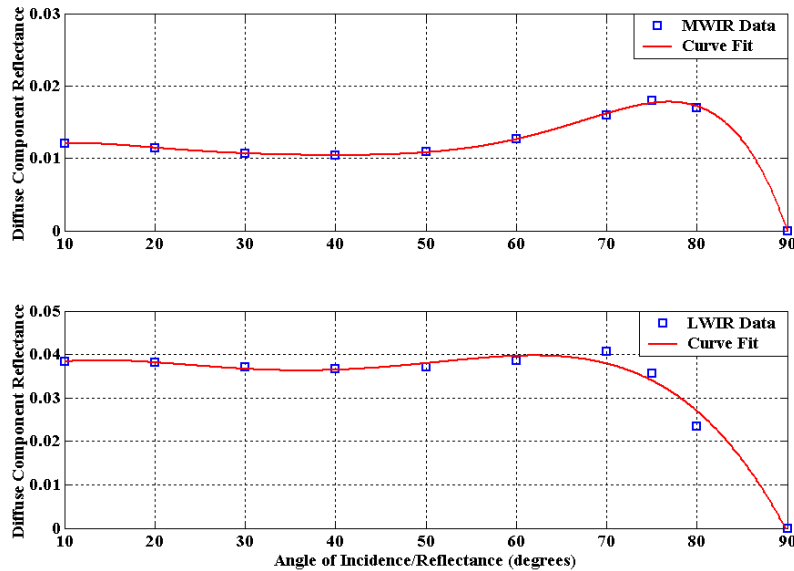

Figure 3-25: The diffuse component reflectance as a function of incident angle. Since the reflectance is so low for both bands, an average reflectance is used for each.

of the paint sample. To answer this question, the OMF also took a bi-directional reflection distribution function (BRDF) measurement of the sample. The measurement was conducted at 3.39 μm at an incident angle of 20º. The results are shown in Figure 3-26. Within 5º of the reflection angle, the BRDF drops three orders of magnitude, indicating that the paint sample is fairly specular. Although this measurement was taken at 3.39 μm, the sample is expected to be even more specular at longer wavelengths [15]. The irregularities that affect the specular nature of the surface become less significant at longer wavelengths. As the angle of incidence increases, the sample becomes even more specular as demonstrated in Figure 3-27 where the sample was measured at 3.39 μm, but at different angles of incidence. As the angle increases, each BRDF peak narrows implying an increase in specularity.
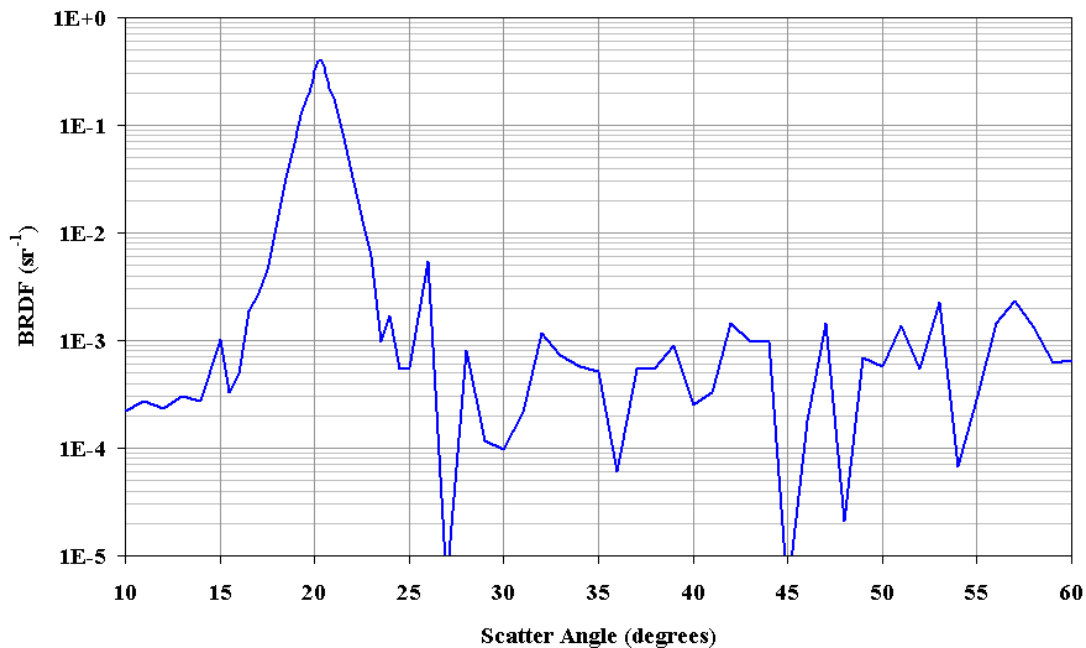

Figure 3-26: The bi-directional reflectance distribution function (BRDF) measurement of the plastic model aircraft paint sample. The BRDF drops three orders of magnitude within 5º of the reflection angle. The measurement was taken at 3.39 μm and at 20º incident angle.
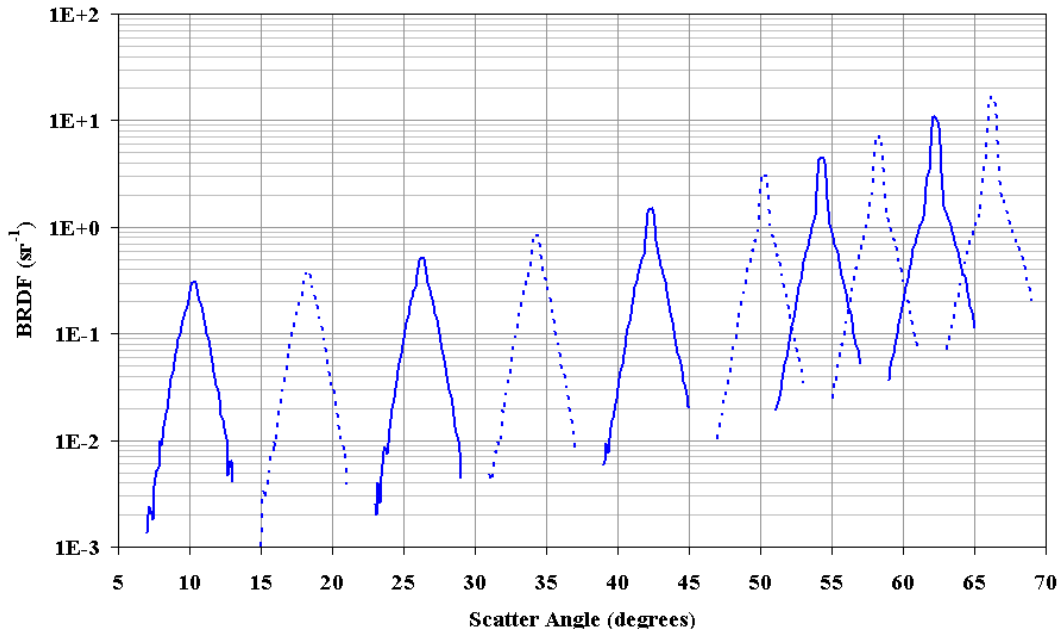
Figure 3-27: BRDF measurements at varying incident angle. As the angle of incidence increases, the peaks narrow signifying an increase the specular nature of the sample.

3.8   Atmospherics

The radiometric model has the capability of computing the aircraft intensity in the absence of an atmosphere (source intensity) or including the effects of the atmosphere (apparent intensity). The atmosphere primarily has two effects on the observed intensity:

1.) It creates a spectral transmission based on atmospheric conditions.

2.) It has a spectral radiance for the path between the observer and aircraft which contributes to the reflected intensity of the aircraft.

To obtain the contributions from these two atmospheric effects, a simulation was conducted utilizing the Philips Lab Expert-assisted User Software (PLEXUS) (Release 3, Version 2), an atmospheric modeling program that incorporates Moderate Transmission Model (MODTRAN), Fast Atmospheric Signature Code (FASCODE), High Resolution Model (HITRAN), SHARC (Strategic High Altitude Atmospheric Radiance Code) and

MODTRAN Merged (SAMM1) and/or SHARC/SAMM Atmospheric Generator (SAG) to generate an atmospheric spectral transmission window and radiance.

Figure 3-28 shows the MWIR spectral transmission window generated by PLEXUS for a path length of 6000 feet with the target 20º above the horizon. The simulated location is Albuquerque, NM at 5355 feet AGL. The simulated time is 9 Dec 04 at 1600 hours in the afternoon. Furthermore, simulated weather conditions are extremely clear and calm with high visibility (50 km), and using a desert aerosol environment with no additional influence from combustion products and industrial agents. Figure 3-29 depicts the MWIR spectral radiance for the atmosphere given the conditions just listed.

Spectral transmission windows and radiances are generated by PLEXUS and saved to data files later accessed by the radiometric model. This methodology allows a large number of atmospheric scenarios to be used by the radiometric model without the need for an interface with MODTRAN.
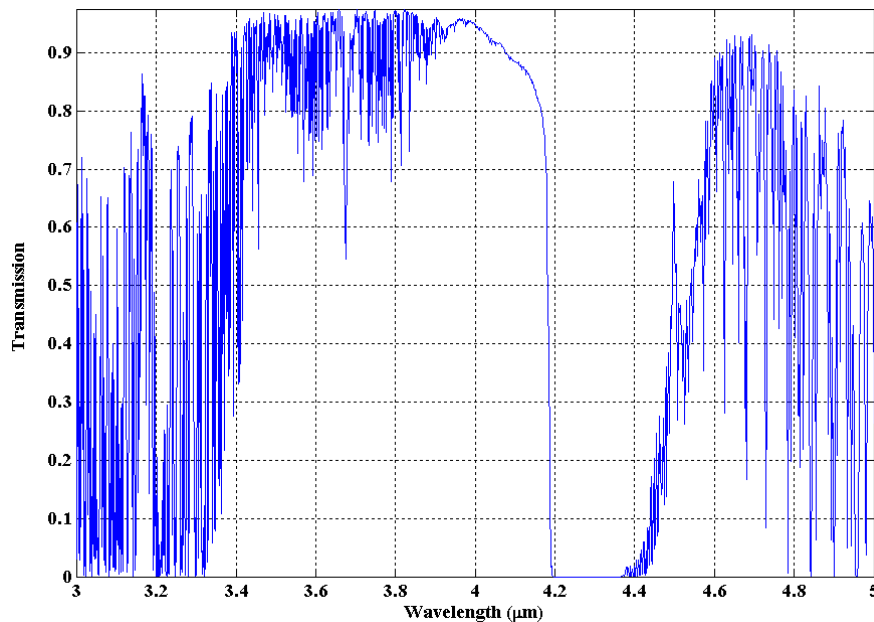

Figure 3-28: An example spectral atmospheric transmission window created by PLEXUS.
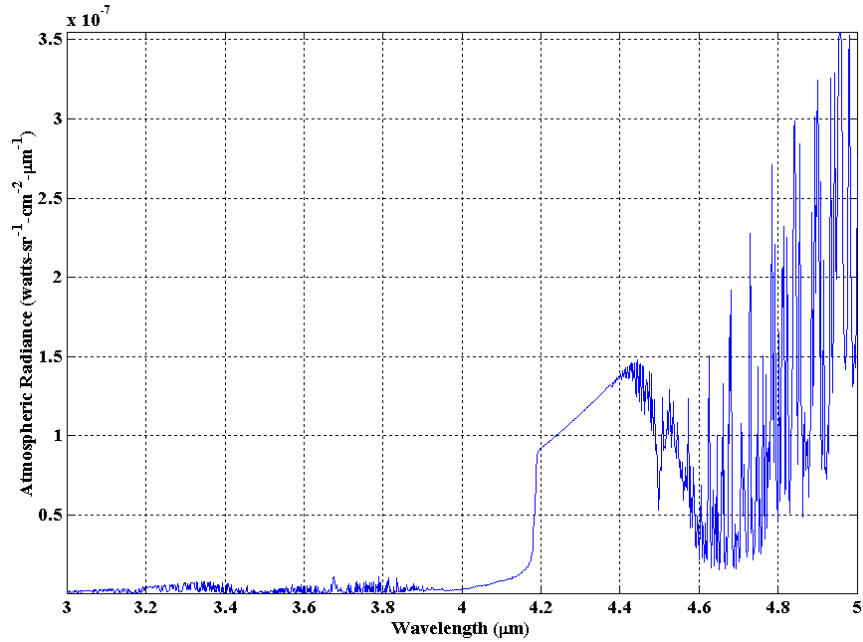
Figure 3-29: An example MWIR spectral radiance of the atmosphere as computed by PLEXUS.

3.9   Radiometric Calculations

The basic assumption in the radiometric computations is that the area of the source is much smaller than the square of the range from the source to the observer $(A_s << R^2)$.   Since the radiance and intensity are being calculated for each facet individually, this is a valid assumption especially since the largest facet area is only 1.15 m^2. A range of only 3.5 m when squared is already greater than ten times the area of the source. This assumption allows the use of Equation (2-13).

$$I_e \cong L_e A_s \cos\theta_s,$$ (Eq 2-13)

As previously discussed, the emissivity of the simple surface is independent of wavelength and angle, while the emissivity for the measured paint sample was angle dependent and wavelength independent. On the other hand, radiance, normalized system

3-32

input response, atmospheric transmission, and atmospheric radiance are all spectral. Equation (2-13) is expanded as follows:

$$I_{facet,self} = A_{facet} \cos\theta_{facet}\varepsilon(\theta_{facet}) \underbrace{\int_{\lambda_1}^{\lambda_2} H(\lambda)\left[\tau_{atm}(\lambda)L_{facet}(\lambda,T) + L_{atm}(\lambda)\right]d\lambda}_{L_{facet,self}}. \quad \text{(Eq 3-14)}$$

Equation (3-14) finds the intensity of a facet due to self-emission. The angle θ_{facet}, is the angle between the facet's normal and the observation line. The angle is also the angle of incidence for that facet. The term, $\varepsilon(\theta_{facet})$, is the emissivity as a function of incident angle for the paint sample. For the simple surface, emissivity is not a function of the incident angle.

H(λ) is the normalized system input response which describes the spectral response of a detection system. A generic normalized system input response is shown in Figure 3-30 alongside the system input response of a MWIR camera using a cold-filtered indium antimonide (InSb) detector. Noting the similarities between the two, the generic response would be appropriate for an InSb detector; however, replacing the generic
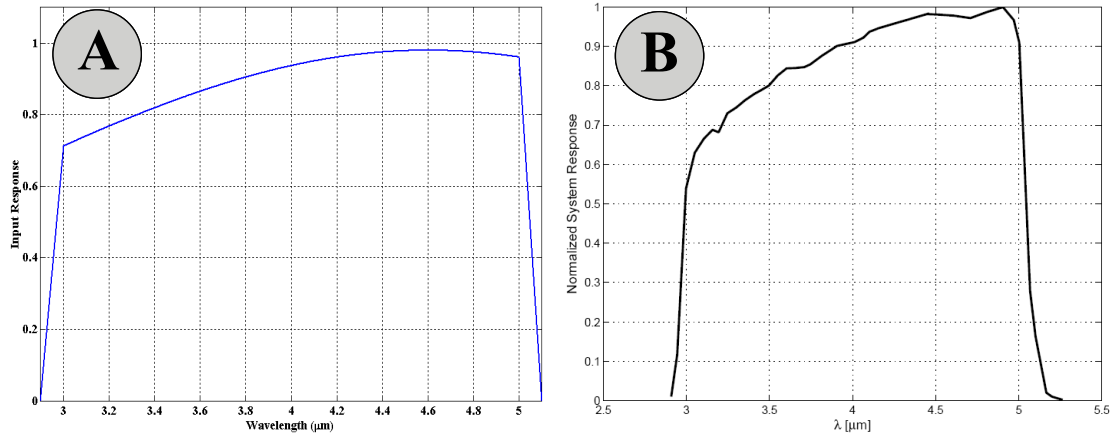

Figure 3-30: **A:** A generic normalized system input response used by the radiometric model. **B:** The normalized system response of a MWIR camera with cold-filtered indium antimonide detector as measured by the Sensors Directorate at the Air Force Research Laboratory, Wright Patterson AFB, Ohio [15].

responses with actual responses would be preferred. Generic responses were used due to lack of access to real data. The radiometric model can access a database of different system input responses, generic or real.

Atmospheric transmission [$\tau_{atm}(\lambda)$] and radiance [$L_{atm}(\lambda)$] have already been discussed and are depicted in Figures 3-28 and 3-29, respectively. The radiance of the facet is determined by *Planck's Radiation Law* as described in Chapter II. Equation (2-16) is used to find the self-emitted spectral radiance of a facet at a given temperature (T) and is depicted in Figure 3-31 for a temperature of 700 K at MWIR.

$$L_{facet}(\lambda, T) = \frac{2hc^2}{\lambda^5 \left(e^{hc/\lambda kT} - 1 \right)} . \qquad \text{(Eq 2-16)}$$

Note that the spectral atmospheric radiance, $\tau_{atm}(\lambda)$, has units of $\dfrac{watts}{sr\ \ cm^2\ \mu m}$, while the
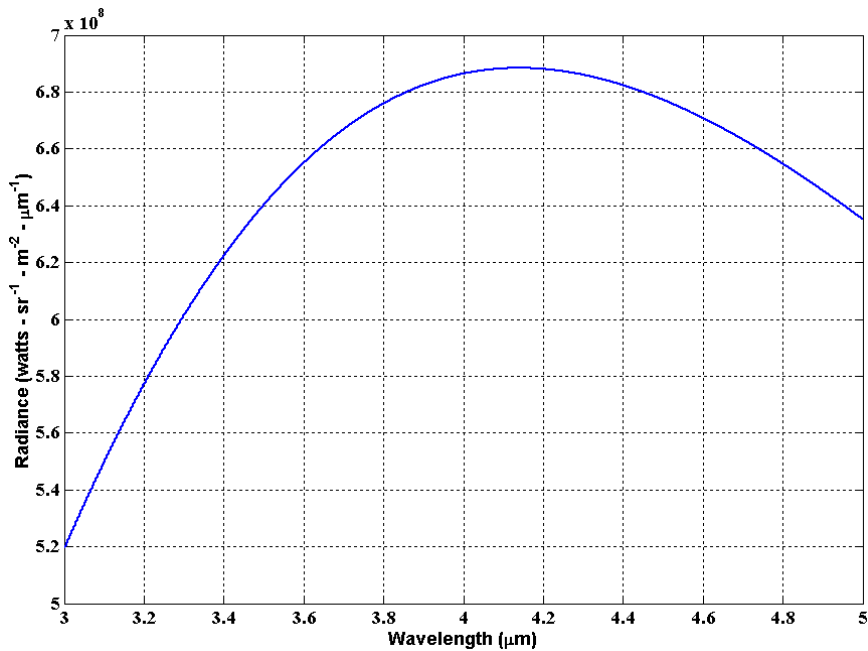

Figure 3-31: The spectral source radiance of a facet at a temperature of 700 K at MWIR.

facet spectral radiance, $L_{facet}(\lambda,T)$, has units of $\dfrac{watts}{sr\ m^2\ \mu m}$. Therefore in Equation (3-14), $L_{atm}(\lambda)$ must be multiplied by a conversion factor of 10,000 to agree with the facet spectral radiance units. Units of m^{-2} are preferred since the area of the facet, A_{facet}, has units of m^2.

The total intensity of a single facet is the sum of the self-emitted intensity, the specular reflected intensity of another facet, earth, or sky, and the diffuse reflected intensity of the earth or sky. The latter is a simplification that assumes only the sky or earth contributes to the diffuse reflected intensity. The determination of which is the contributor is wholly based on the orientation of the facet, much like the earth and sky shine segment of the reflection algorithm. In reality, a 2π steradian hemisphere of rays would contribute to the diffuse reflected intensity. The rays could originate from other facets, the earth, the sky, or any combination of the three. The total intensity is therefore,

$$
\begin{aligned}
I_{facet,total} = &\; I_{facet,self}\\
&+ \underbrace{A_{facet}\cos\theta_{facet}\rho_{spec}\left(\theta_{facet}\right)\varepsilon_{facet2,\ earth,\ or\ sky}\left(\theta_{facet2}\right)L_{(facet2,self),\ earth,\ or\ sky}}_{I_{specular}} \quad \text{(Eq 3-15)}\\
&+ \underbrace{A_{facet}\cos\theta_{facet}\rho_{diff}\left(\theta_{facet}\right)L_{earth\ or\ sky}}_{I_{diffuse}}
\end{aligned}
$$

The radiance term in the $I_{specular}$ calculation is either the facet self emission as computed in the integral of Equation (3-14), the emission from the earth, or the emission from the sky. Consequently, the emissivity term is that for the reflected facet (facet 2), the earth or the sky (the earth and sky emissivities are both 1.0). Once again, the emissivity for the reflected facet is dependent on incident angle for the paint sample, but not for the simple surface case. The specular reflectance (ρ_{spec}) for the facet is computed using Equations

3-35

(3-11) or (3-12), depending on IR band, for the paint sample. For the simple surface, the specular reflectance is set to a user-defined value. An averaged diffuse reflectance (ρ_{diff}) for the paint sample of 0.0127 for MWIR and 0.0377 for LWIR was used as previously discussed in Section 3.7. For the simple surface, ρ_{diff} is simply $1-\rho_{spec}$.

3.10 Summary

Chapter III developed the radiometric model from the ground up. The faceted model is created using MATLAB® techniques and geometric equations. Understanding how facets were created allowed representation of those facets using vectors, which then permitted use of vector operations and vector math to find facet normals, areas, and angles of incidence. Using those basic concepts, an obscuration algorithm was used to create a matrix of facets visible to the observer. Similarly, a reflection matrix was created to include the effects of reflections from parts, earth, or sky. In order to account for self emission and reflection, the surface properties for each facet must also be known. The model can either utilize a simple surface approach where emissivity and reflectance are not functions of incident angle or a more realistic approach based on material measurements. A particular paint sample was chosen for the plastic model aircraft with validation of the radiometric model in mind. The reflectance and specularity of the paint sample was measured and incorporated into the radiometric model. An atmospheric modeling interface was used to create atmospheric scenarios used in determining the apparent intensity of the aircraft. Finally, all segments of the radiometric model are taken into account during the radiometric calculations to find the aircraft's intensity at a given elevation angle and for 360º in azimuth. However, the radiometric model is still not the

easy-to-use desktop tool described in the thesis objective. The graphical user interface

(GUI) described in the next section was developed to fulfill the thesis objective.

IV Graphical User Interface (GUI)

4.1   Overview

A graphical user interface (GUI) was designed in order to examine the effects on aircraft intensity as a result of changing variables in the radiometric model. The GUI can display aircraft component intensities as well as their contributions to the overall intensity of the aircraft. A faceted model viewer allows the user to examine the radiance of the aircraft and its parts at a given aspect angle. This GUI is essentially the desktop tool envisioned for this thesis.

4.2   Main GUI Window

MATLAB$^{®}$ provides a palette for creating GUI's using the *guide* command. Text boxes, check boxes, push buttons, and drop-down lists are a few of the items that can be added to the GUI palette.   When saved, the palette automatically creates call-back functions for each of the GUI items. These call-back functions can then be modified to perform specific tasks. The GUI, titled "Large Commercial Aircraft IR (LCAIR)", is shown in Figure 4-1 (a larger image is located in Appendix D).

4.3   Temperature Selection

This section of the GUI allows the user to control the temperature for all aircraft parts. In many cases, each part has a top and bottom surface that can be set to different or equal temperatures. There is also a push button that allows the aircraft fuselage, wings, stabilizers, and windshield to be set to the same temperature. Engine parts, however, must be set individually. Finally, the earth and sky temperatures can also be set in this section. An assumption is made that both the earth and sky are Lambertian hemispheres with a constant temperature throughout.
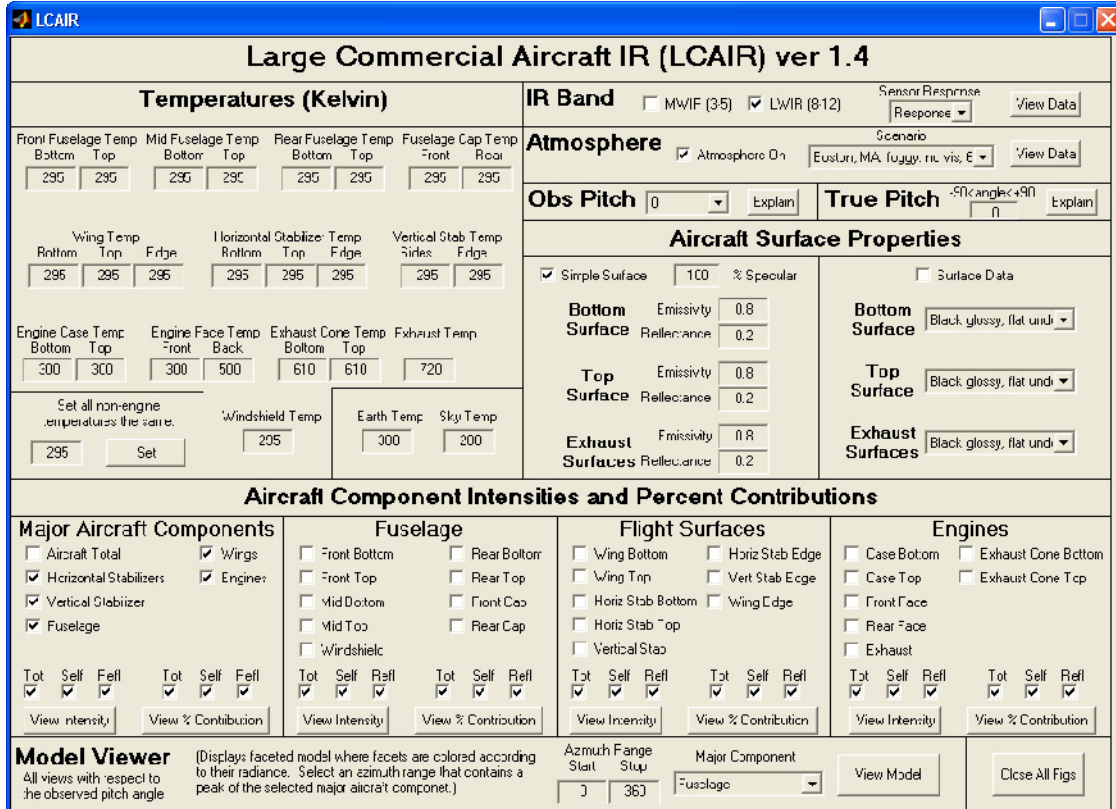
Figure 4-1: The large commercial aircraft IR (LCAIR) GUI. This GUI allows a user to change variables to the radiometric model and examine resultant aircraft and/or component intensities and contributions. The geometric model can also be viewed with facets colored according to their radiance.

4.4 Detector Parameters

The next section of the GUI allows the user to set the IR band the detector is operating in, as well as a normalized input response. Only two bands can be selected: MWIR from 3-5 μm and LWIR from 8-12 μm. There are currently four choices for the normalized input response, but many more can be added. The four choices are generic in nature and meant for demonstration only. Selecting the *View Data* button generates a graph of the response selected. Figure 3-30A is an example of one of the normalized input responses available through the GUI. All available generic normalized input

responses are shown in Appendix B. Realistic system input responses for various detectors or systems can be added in the future.

4.5 Atmospheric Inputs

This section allows the user to incorporate atmospheric effects (or lack of) as described in Chapter III. If the *Atmosphere On* check box is not selected, the radiometric model computes the source intensity for the aircraft and its components. Selecting the box introduces the effects of atmospheric transmission and atmospheric radiance. Presently, there are five atmospheric scenarios that can be accessed by the model, but more can be added. These atmospheric scenarios were created using PLEXUS and intentionally do not represent actual operational conditions to avoid presenting any sensitive information. Each scenario sets the target at a range of 6000 feet and 20º above the horizon. Location, timing, and weather conditions are varied in each scenario to demonstrate their effects. All atmospheric scenarios are listed in Appendix A. Selecting the *View Data* button will produce graphs of the atmospheric transmission window and atmospheric radiance for the selected scenario as in Figures 3-28 and 3-29.

4.6 Aircraft Angles

There are two aircraft angles that the user can control: the observed pitch angle and the true pitch angle. The observed pitch is the apparent pitch of the aircraft as seen by the observer. It can also be thought of as the angle between the aircraft waterline and the observation line. The obscuration and reflection algorithms are highly dependent on the observation pitch angle. Since the algorithms are computationally intensive, obscuration and reflection matrices were created for several observed pitch angles. The user can select an observed pitch angle of -20º, -15º, -10º, -5º, 0º, 5º, 10º, 15º, or 20º

using the drag down menu. The true pitch angle of the aircraft is the angle between the aircraft waterline and the horizon. This is generally just called the pitch of the aircraft. The obscuration and reflection algorithms are not dependent on the true pitch of the aircraft. Therefore, any angle between -90º and +90º can be entered by the user. The true angle has an effect on the amount of earth and sky shine reflected off the aircraft as previously discussed and illustrated in Figure 3-19. Figure 4-2 demonstrates the difference between observed pitch and true pitch.

4.7   Surface Properties

There are two surface property selections available to the user. The first is termed a *simple surface*. This simple surface is further broken down into top, bottom, and engine (washer interface, exhaust cone, and exhaust disk) surfaces. The concept is that some commercial aircraft have paint schemes where the top and bottom are different colors. Emissivity and reflectance are independent of angle and can be set for each of the three surfaces. The percentage of specularity scales the input reflectance value to produce ρ_{spec}
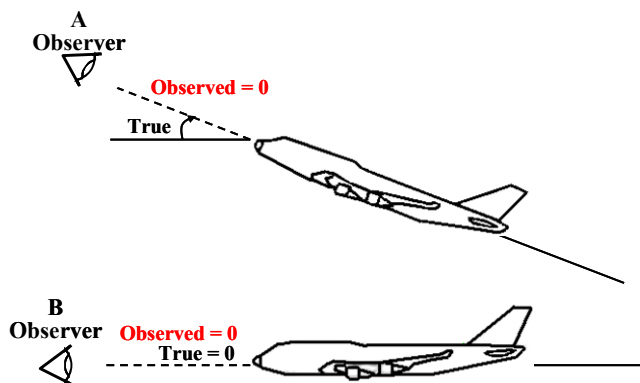
Figure 4-2: The observed pitch angle is the angle between the aircraft waterline and the observation line. On the other hand, the true pitch angle is the angle between the aircraft waterline and the horizon. In **A**, the observed pitch is zero, but the true pitch is a positive angle ~30º. In **B**, both angles are zero.

used in Equation (3-15).

The user can also choose to use paint data obtained through hemispherical diffuse reflectance (HDR) measurements. Angular dependent functions for the emissivity and reflectance are derived from the data as described in Section 3.7. The only paint data currently available is for the Krylon, 1601, glossy black.

4.8   Component Intensities and Contributions

This section generates the main outputs of the radiometric model based on variables set in the other sections. The intensity and contribution of components can be examined grouped together as a major aircraft component or individually. Additionally, the overall intensity of a component can be further broken down to self-emission and reflected intensities.

Using the conditions set in Figure 4-1 (LWIR, atmosphere on, 0º observed pitch, etc.) then selecting *View Intensity* under the *Major Aircraft Components* section produces the overall intensity chart shown in Figure 4-3. The intensities for the fuselage, wings, vertical stabilizer, and horizontal stabilizers as shown in Figure 4-3 are primarily functions of their projected areas. The fuselage presents the largest area when viewed from broadside (90º and 270º) – the same holds true for the vertical stabilizer. The wing and horizontal stabilizer intensities have the same form since the horizontal stabilizers are essentially small wings and are positioned in the same way. The wing and horizontal stabilizer intensities seen from the front of the aircraft are a result of their respective leading edges. When viewed from the rear (180º), the top portion of the wings and horizontal stabilizers contribute to the intensity. Finally, since the rear part of the engines is the hottest, it is logical that the engine intensity increases as the azimuth approaches
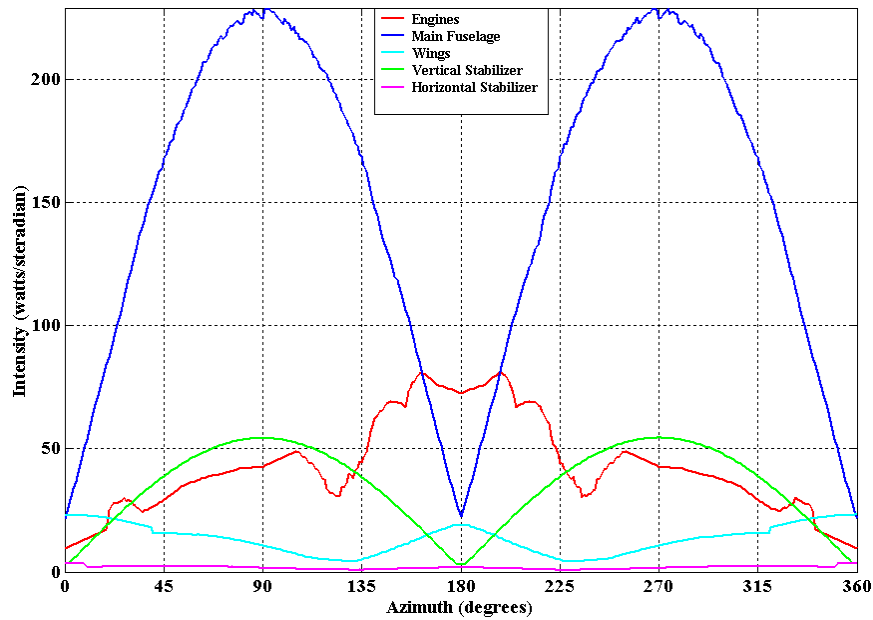
4-5

Figure 4-3: Apparent intensity as a function of azimuth angle for major aircraft components. The simulation is conducted at LWIR, 8-12 μm, with an aircraft observed/true pitch of 0º. Other conditions are set as in Figure 4-1.

180º. The notch seen at 125º is caused by the outer engine obscuring the inner engine. Numerical maximums and minimums for part intensities are also printed to the MATLAB® command window.

Although the intensity of the engines is less than the intensity of the fuselage, the radiance of the engines is not necessarily less than the radiance of the fuselage. Recall that Equation (2-13) shows that intensity is the product of the radiance and the projected area of the source. Consequently, a large area like the cool fuselage can result in a higher intensity than a smaller area such as the hot engines. Figure 4-4 (generated by the faceted model viewer which will be discussed later) presents the model with facets colored according to their radiance. A higher radiance results in a lighter color as depicted in the color bar. It is evident from this picture that the engines have a higher radiance than the

Apparent Radiance, at EL = 0°, Az = 90°, (longwave IR, 8-12 μm)
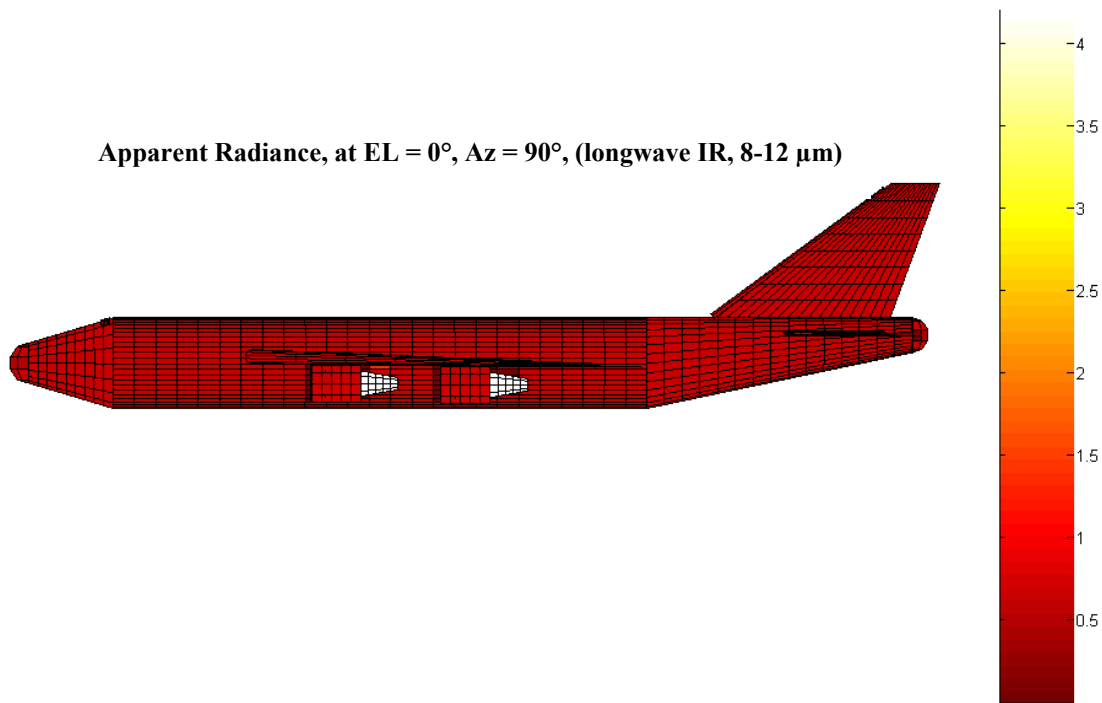
Figure 4-4: Broadside view of the faceted model. Facets are colored by their radiance. Higher radiance results in a lighter color. Since intensity is a radiance/projected area product, the fuselage has a higher intensity due to its large projected area. The engines have a lower intensity despite having a higher radiance since their projected area is much less.

fuselage but also much less projected area. The resulting intensity is lower for the engines than for the fuselage as portrayed in Figure 4-3.

The intensities shown in Figure 4-3 are the total intensities for each aircraft part. These intensities can be further broken down into self emission and reflected portions as depicted in Figure 4-5. The reflected intensity represents other aircraft parts, earth shine, and/or sky shine reflecting off the specified aircraft component. At longer wavelengths, the earth and sky shine can be fairly significant as demonstrated in the figure (note that the graphs in Figure 4-5 are each scaled differently).

Self Emission   **Reflected**
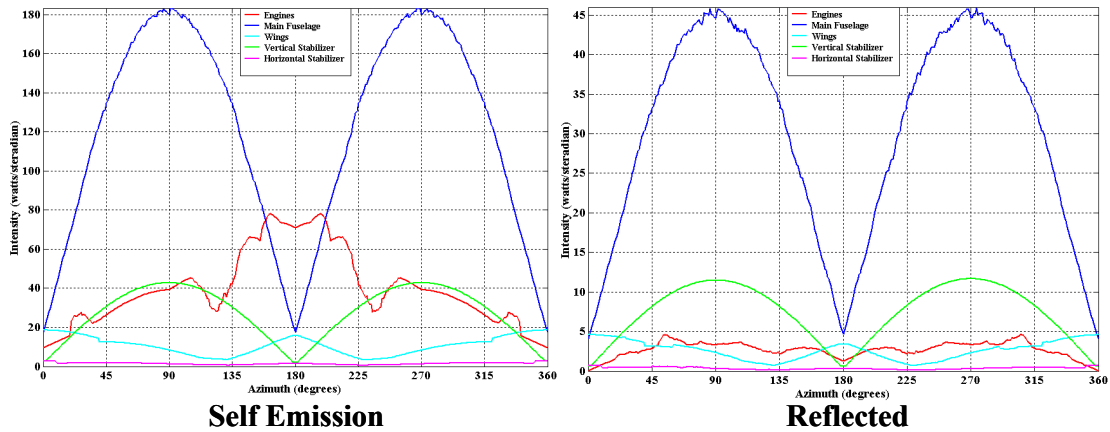
Figure 4-5: Total intensity of each part can be broken down into a self emission component and reflected component. At long wavelengths, earth and sky shine contribute a significant amount to the total intensity of the aircraft. Notice each graph is scaled differently.

The intensity of each selected component is compared to the total intensity of the aircraft to determine the contribution of each part. The result is plotted in Figure 4-6. As with the intensity, the amount of contribution of each part can be further broken down into self emission and reflected components as shown in Figure 4-7.
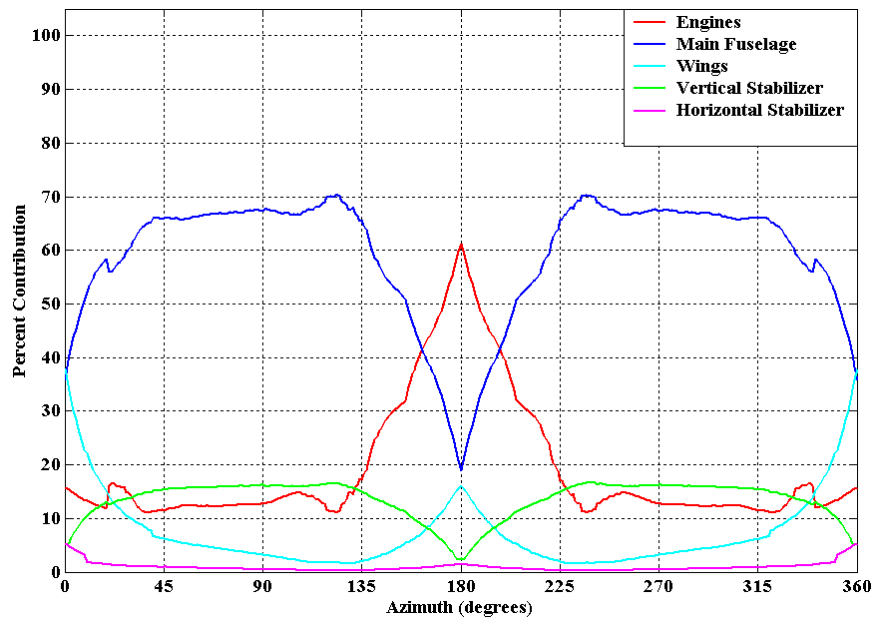
Figure 4-6: The percent contribution of each major aircraft component to the overall intensity of the aircraft.

Self Emission   **Reflected**
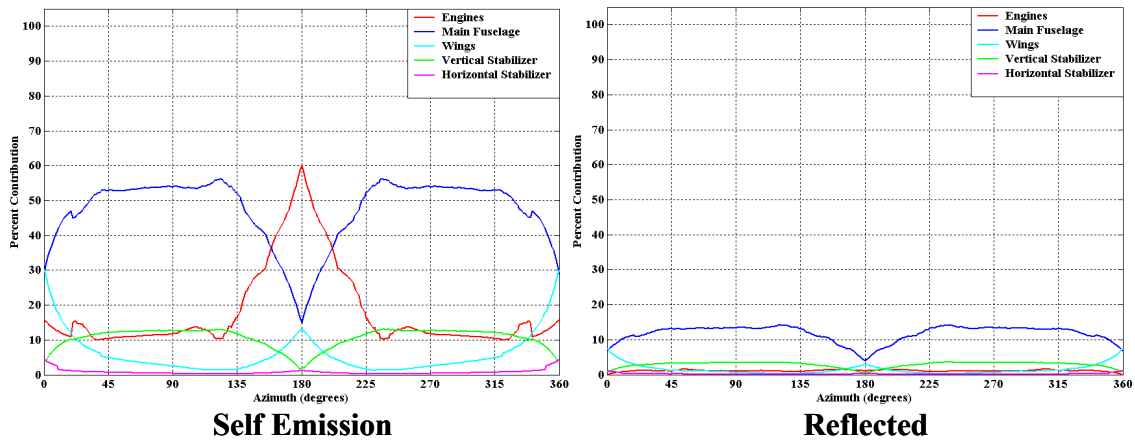
Figure 4-7: The self emission and reflected contributions to the overall aircraft intensity. Parameters are set as in Figure 4-1 (LWIR, 0º pitch, etc).

The reflected intensity contributes up to an additional 14% to the overall aircraft intensity over a broad range of azimuth angles due to reflections off the fuselage alone.

The example used to create Figures 4-3 through 4-7 is just one of many possible scenarios using this GUI. Effects of a particular parameter can be examined by keeping all other parameters the same and changing just that one. For example, to study the effects of the "Foggy Boston" atmospheric scenario, the intensity is plotted with the atmosphere on and off in the longwave IR band. The results are plotted in Figure 4-8.

No Atmosphere (source intensity)   **With Atmosphere (apparent intensity)**
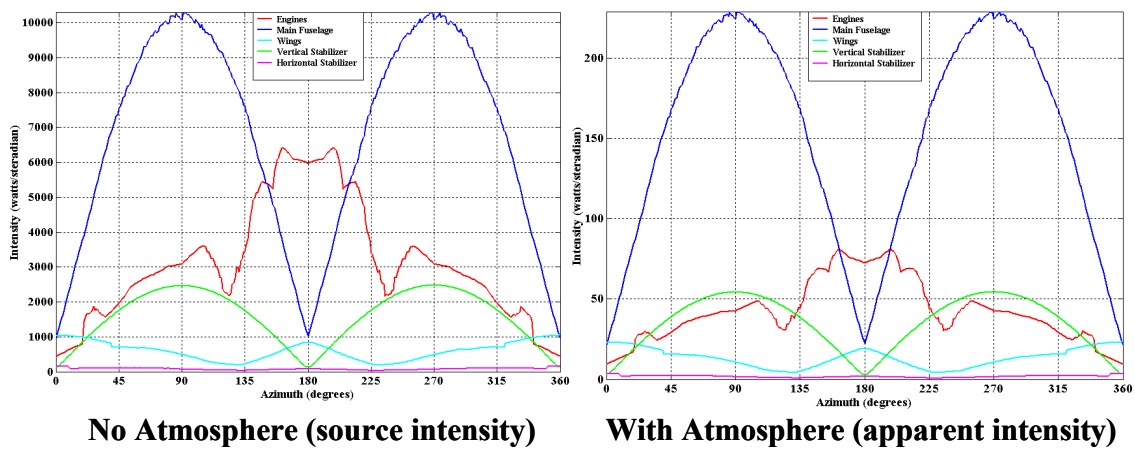
Figure 4-8: The intensity of major aircraft components with and without effects of the "Foggy Boston" atmospheric scenario. Note the scaling of the magnitudes.

The atmospheric attenuation is quite severe resulting in a drastic decrease in magnitude. However, the attenuation is even more severe for the engines than for any other part. In fact, the other aircraft components are proportionally the same in both plots. Since the cool aircraft parts are all at the same temperature, they have the same spectral radiance. Therefore any spectral attenuation function would affect all of those parts the same. As the blackbody curves in Chapter II showed, warmer bodies peak at shorter wavelengths. Therefore, the warmer engines will be affected differently by the atmospheric attenuation.

4.9   Faceted Model Viewer

The intensity and percent contribution plots are great analytical tools especially since they provide full azimuth data. However, sometimes these plots lack the physical insight as to the cause certain features. To address this, the GUI can portray the faceted aircraft with the facets colored according to their radiance. Coloring the facets based on their radiance provides a better contrast than plotting the intensity, which is the radiance multiplied with the projected area. This type of figure assists in identifying hot parts, reflections, and obscurations but obviously can only display one azimuth angle at a time. To view a specific angle, the user can enter the same azimuth angle in the start and stop text windows. Otherwise, the GUI finds the peak intensity for the selected part within the selected range. For example, Figure 4-9 shows the intensity of the fuselage at MWIR with the aircraft at 20º pitch, and no atmospheric effects. The intensity of the fuselage has quite a bit of jaggedness caused by reflections of hot engine parts off the fuselage. The faceted model viewer allows the user to examine a peak to ascertain the cause or validity of the peak. In Figure 4-9, a small peak somewhere between 0º and 10º is
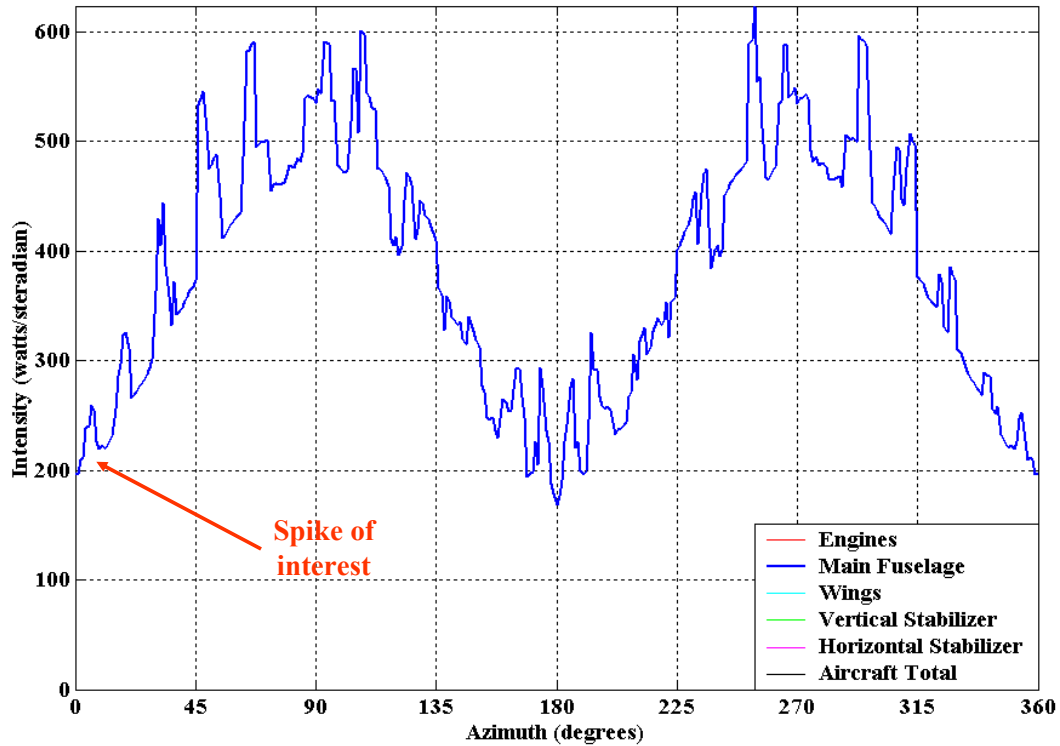
Figure 4-9: The fuselage intensity for an aircraft at MWIR, 20º pitch, no atmospheric attenuation. The jaggedness of the signal is caused by reflection of hot engine parts off the fuselage. One peak is singled out for inspection.

singled out for inspection. Selecting the fuselage as the major component to examine, entering a range of 0º to 10º, and then pressing the *View Model* button results in Figure 4-10.

The first piece of information that can be gleaned from Figure 4-10 is that the peak intensity of the fuselage occurs at 6º given the inputs entered. The next obvious feature is the engine reflection off the fuselage. Even though the engine hot parts are not visible to the viewer, their reflections may be. Notice, there is also another small reflection on the fuselage just left of the primary reflection.
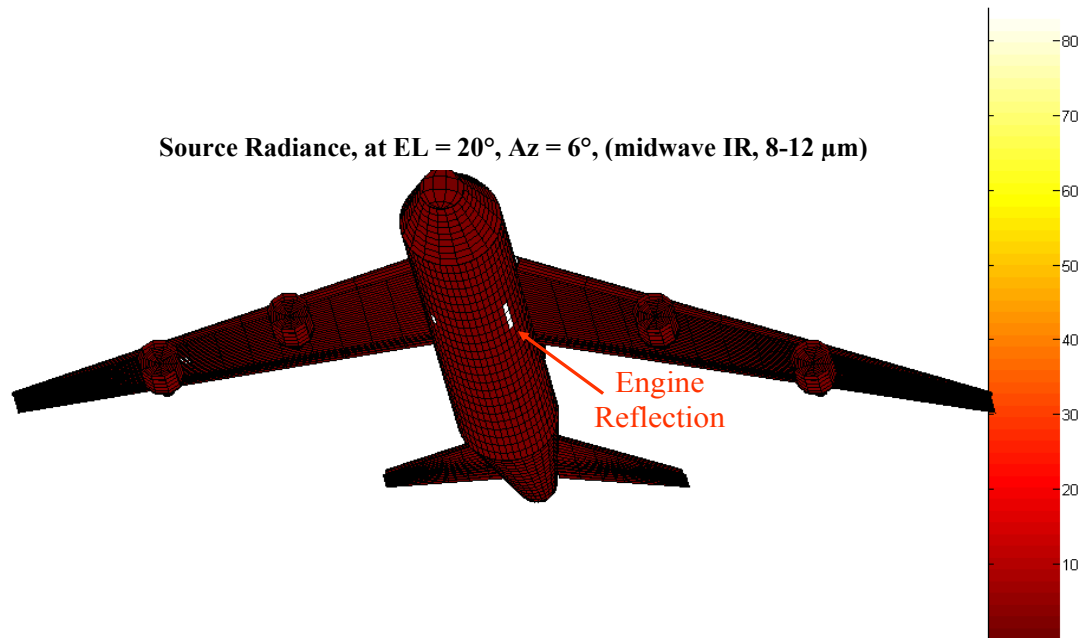
Figure 4-10: The image created by the faceted model viewer to examine the spike of interest from Figure 4-9. Even though the engine hot parts are not viewable by the observer, their reflections are.

4.10 Summary

The graphical user interface, with the radiometric model at its core, satisfies the objective of developing a desktop tool capable of identifying IR signature trends. The user can control aircraft part temperatures, IR band of interest, normalized input system response, atmospheric scenarios or lack of atmosphere, aircraft angles, and surface properties. Real input responses, atmospheric scenarios, and paint schemes can be added for operationally realistic analysis. The output intensity graphs include total, self-emission, and reflection signatures for the aircraft or its components. This is particularly useful in determining the source of a particular signature trend; whether it is due to self emission or reflection. Finally, the faceted model viewer provides additional insight into signature trends by depicting the faceted model colored by its radiance.

There are certainly improvements that can be made to the radiometric model, but more importantly, the model must be validated to determine the amount of error between the computational model and a physical model. Model validation and other recommendations are discussed in the next chapter.

V Recommendations and Conclusions

5.1   Overview

There are several recommendations for future work, but none are more important than model validation. Model validation is necessary to determine the amount of error in the radiometric model and whether it is useful as a trend analysis tool. Plume modeling, MODTRAN interface, spectral data access, and obscuration/reflection algorithm improvements make up the other recommendations and are listed in order of importance after model validation.

5.2   Model Validation

Of the recommendations for future work on this thesis, model validation is the most crucial. As previously mentioned, the desktop tool created as a result of this thesis is a trend analysis tool. It was not intended to be as precise as other existing IR codes. By identifying trends, the user can then focus their efforts using more robust IR codes.

Even as a trend analysis tool, a certain level of confidence is required in the model. This is where model validation is required. As mentioned in Section 3.7, a 1:100 scale plastic model of a 747-400 was acquired and painted gloss black for model validation. However, it was determined that even with the insulation, the plastic model would cool too quickly. Heater strips were considered, but even then temperature control would be difficult to maintain. Due to these concerns, validation with the plastic model was not accomplished.

An alternative to the plastic model is to use a plumbed (for temperature control), simply-shaped model for validation. The model should still consider surface interactions by using multiple parts. This would exercise the obscuration and reflection algorithms

used in the radiometric model. Of course, this would require a new faceted model be created using the concepts presented in Chapter III. New obscuration and reflection matrices would also need to be generated.

Regardless of the physical model used for validation, the challenge would be in correlating the data from the IR range with that produced by the radiometric model described in this thesis. Errors and limitations inherent in the IR range measurements would have to be considered when comparing the data.

5.3 Plume Modeling

The effects of the plume were not considered in the radiometric model. The plume's radiance, reflections off aircraft components, and plume self-absorption should be incorporated into the model. The added contribution from the plume would be more significant at the midwave IR band. Plume modeling would require an understanding of the radiometry of hot gases and gas flows.

5.4 MODTRAN Interface

Currently, the sky and earth are both assumed to have Lambertian radiances based on constant temperatures. For added realism, the sky and earth spectral radiances can be calculated by PLEXUS and incorporated into the model. Also, the atmospheric path from the aircraft to the earth based on its altitude is currently not considered when determining earth shine. While this thesis project avoided using a direct interface with MODTRAN, such an interface may be required to increase the fidelity of the model.

5.5 Spectral Data Access

Presently all spectral data is integrated early in the process then assigned to each facet as its radiance. Furthermore, projected area analysis and angle-dependent surface

properties are applied to each facet for an azimuth range of 0º to 360º. The resulting data is stored and manipulated as a 5791 (number of facets) by 361 (azimuth range) matrix. Further insight could be gleaned by carrying the spectral data to the end. This would require a 3-D matrix where the third dimension is determined by the spectral resolution.

5.6   Obscuration and Reflection Algorithms

Using a radiosity or ray-casting approach to create the obscuration and reflection matrices would eliminate the errors inherent in the algorithms used for this thesis. However, if validation determines that the overall model error is acceptable, then correcting these algorithms is not of high priority.

5.7   Conclusion

The recommendations provided in this chapter will make the overall model more robust, but may increase computational times. The same is true for increasing the faceted model resolution to minimize facet area errors. Care should be taken to avoid straying too far from the purpose of thesis.

The objective of this thesis was to develop a desktop tool capable of identifying IR signature trends of a large commercial aircraft. The graphical user interface, using the radiometric model as its computational engine, is that tool. The 360º intensity graphs display the IR signature trends of the aircraft as a whole or by part contribution. Additionally, the specific IR signature can be broken down into self emission and reflection components to further isolate the source of the signature. And finally, the faceted model viewer provides additional physical insight into the cause of signature phenomenon. As intended, planners can focus their use of robust IR codes to accurately evaluate IR signatures based on the trends produced by the radiometric model.

Appendix A PLEXUS-Generated Atmospheric Scenarios

Table A-1: Atmospheric Scenario #1

| Simulation Variable	Setting/Value
IR Band	MWIR/LWIR
LOS definition	Sensor geometry
Path length	6000 ft
Azimuth angle	20º
Zenith angle	70º
Location	Las Vegas, NV
Location altitude	2205 ft
Date	9 Dec 04
Time	1600
Weather conditions	Clear day/no significant changes
Visibility	Low visibility, 1km
Aerosol environment	Desert
Industrial influence	Direct influence
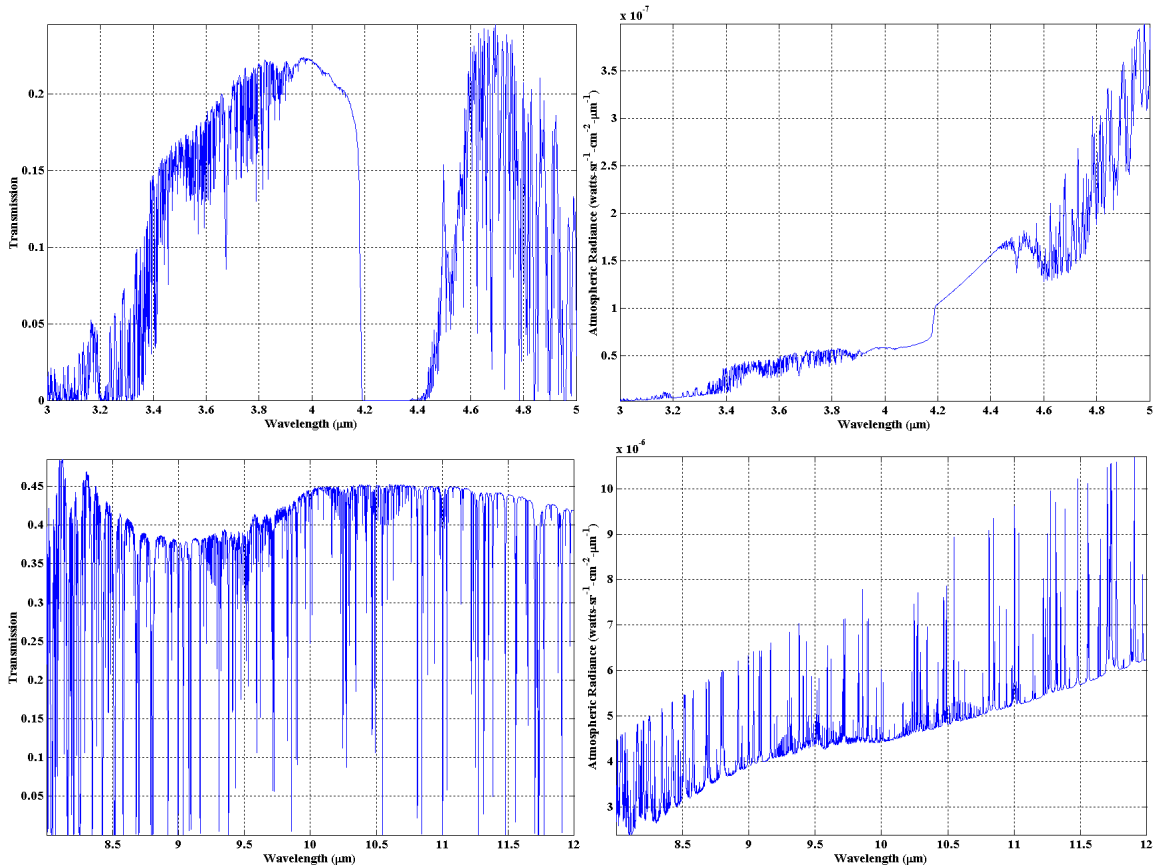
Figure A-1: MWIR/LWIR spectral atmospheric windows and path radiances for Scenario #1. Conditions are listed in Table A-1.

Table A-2: Atmospheric Scenario #2

Simulation Variable	**Setting/Value**
IR Band	MWIR/LWIR
LOS definition	Sensor geometry
Path length	6000 ft
Azimuth angle	20º
Zenith angle	70º
Location	Biloxi, MS
Location altitude	34 ft
Date	9 Dec 04
Time	2200
Weather conditions	Night/just rained
Visibility	Normal low visibility, 5km
Aerosol environment	Maritime
Industrial influence	N/A
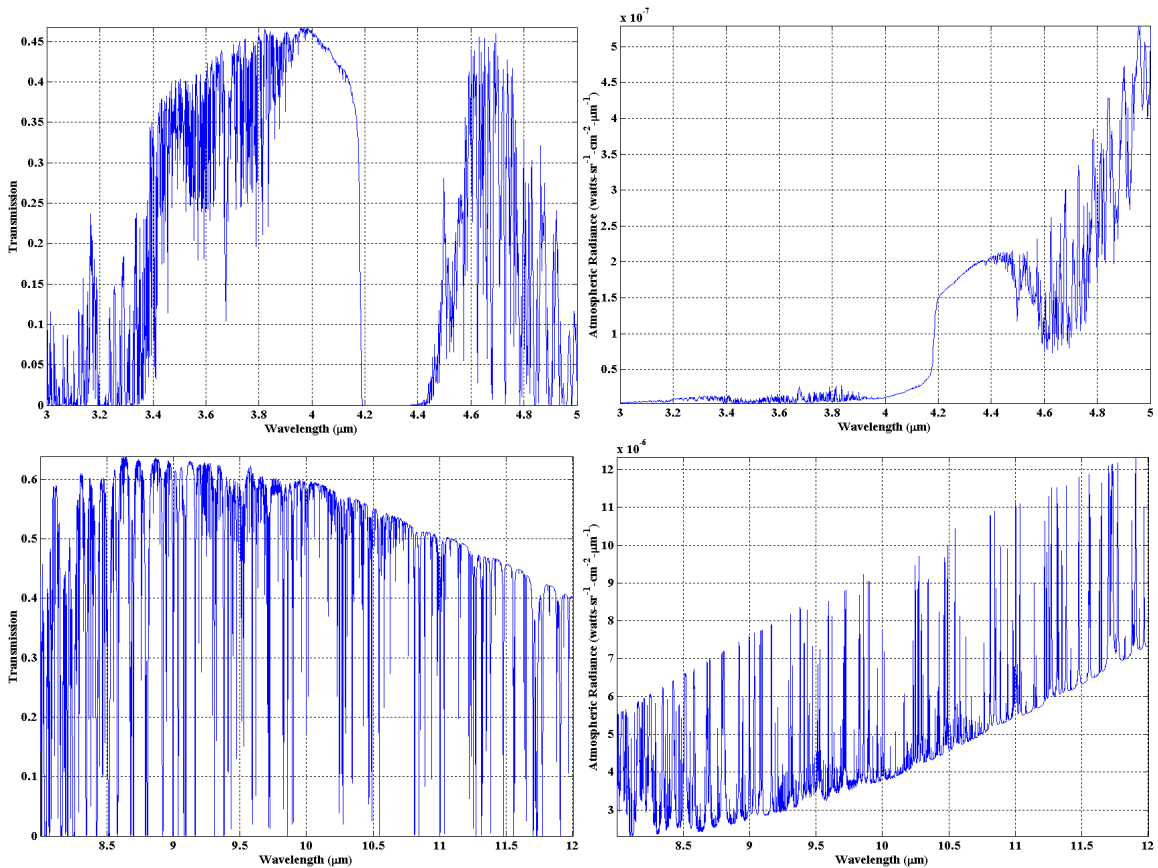
Figure A-2: MWIR/LWIR spectral atmospheric windows and path radiances for Scenario #2. Conditions are listed in Table A-2.

Table A-3: Atmospheric Scenario #3

Simulation Variable	Setting/Value
IR Band	MWIR/LWIR
LOS definition	Sensor geometry
Path length	6000 ft
Azimuth angle	20º
Zenith angle	70º
Location	Boston, MA
Location altitude	19 ft
Date	9 Dec 04
Time	0800
Weather conditions	Foggy day
Visibility	Extremely low visibility, 0.2km
Aerosol environment	N/A
Industrial influence	N/A
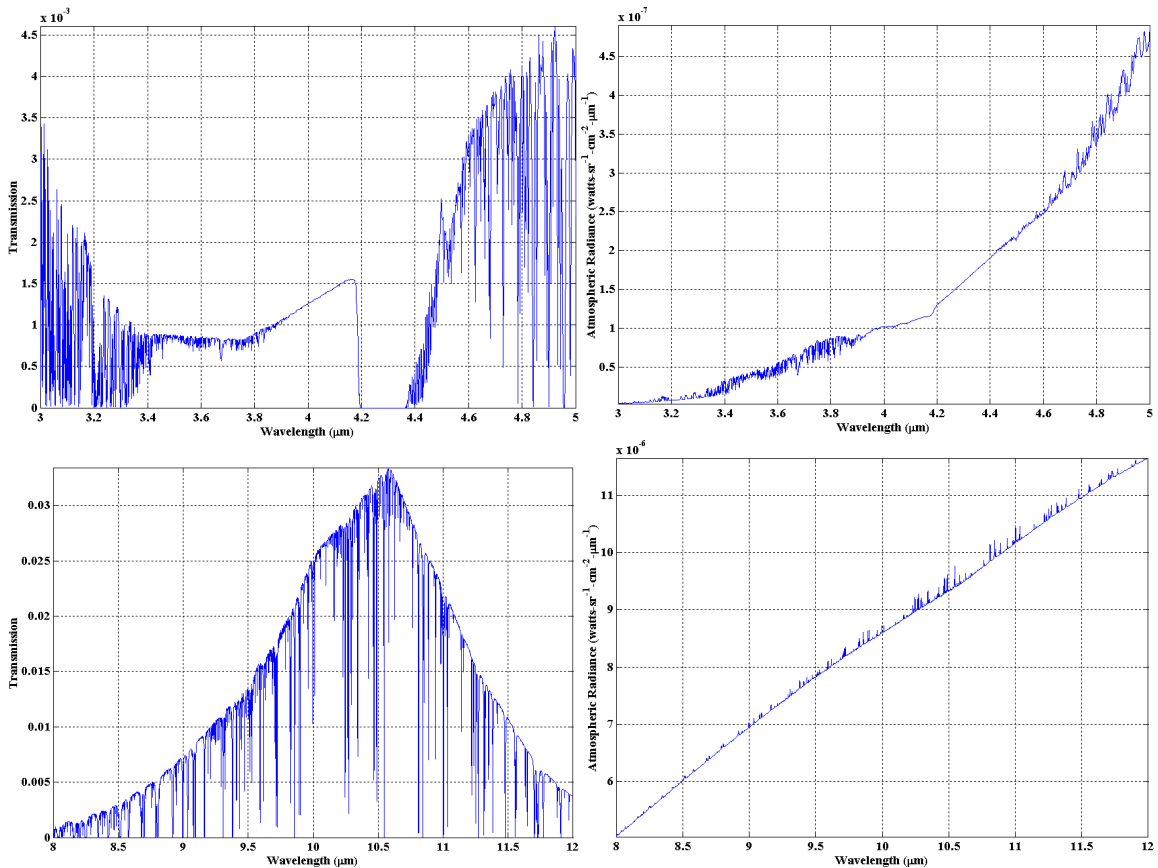
Figure A-3: MWIR/LWIR spectral atmospheric windows and path radiances for Scenario #3. Conditions are listed in Table A-3.

Table A-4: Atmospheric Scenario #4

Simulation Variable	Setting/Value
IR Band	MWIR/LWIR
LOS definition	Sensor geometry
Path length	6000 ft
Azimuth angle	20º
Zenith angle	70º
Location	Los Angeles, CA
Location altitude	126 ft
Date	9 Dec 04
Time	1600
Weather conditions	Clear day/no significant weather
Visibility	Normal low visibility, 5km
Aerosol environment	Urban
Industrial influence	N/A
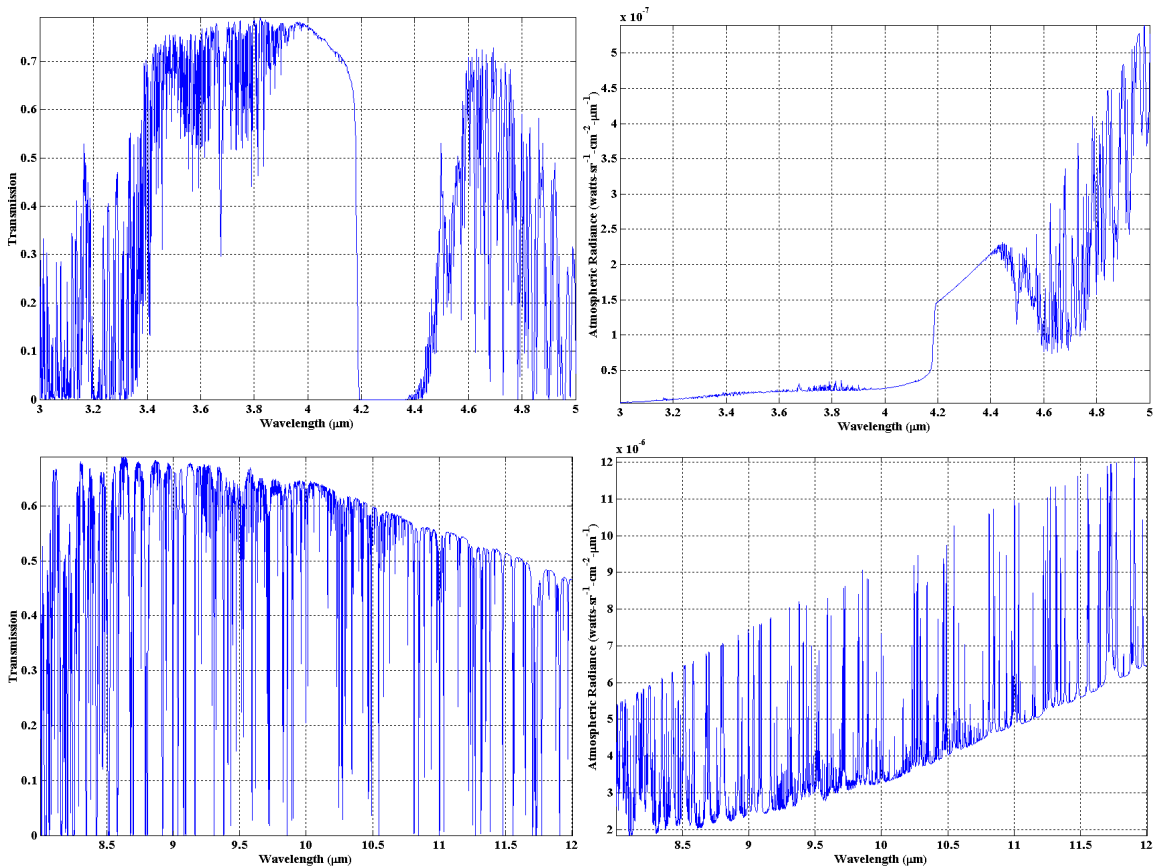
Figure A-4: MWIR/LWIR spectral atmospheric windows and path radiances for Scenario #4. Conditions are listed in Table A-4.

Table A-5: Atmospheric Scenario #5

Simulation Variable	Setting/Value
IR Band	MWIR/LWIR
LOS definition	Sensor geometry
Path length	6000 ft
Azimuth angle	20º
Zenith angle	70º
Location	Albuquerque, NM
Location altitude	5355 ft
Date	9 Dec 04
Time	1600
Weather conditions	Clear day/extremely clear and calm
Visibility	High visibility, 50km
Aerosol environment	Desert
Industrial influence	None
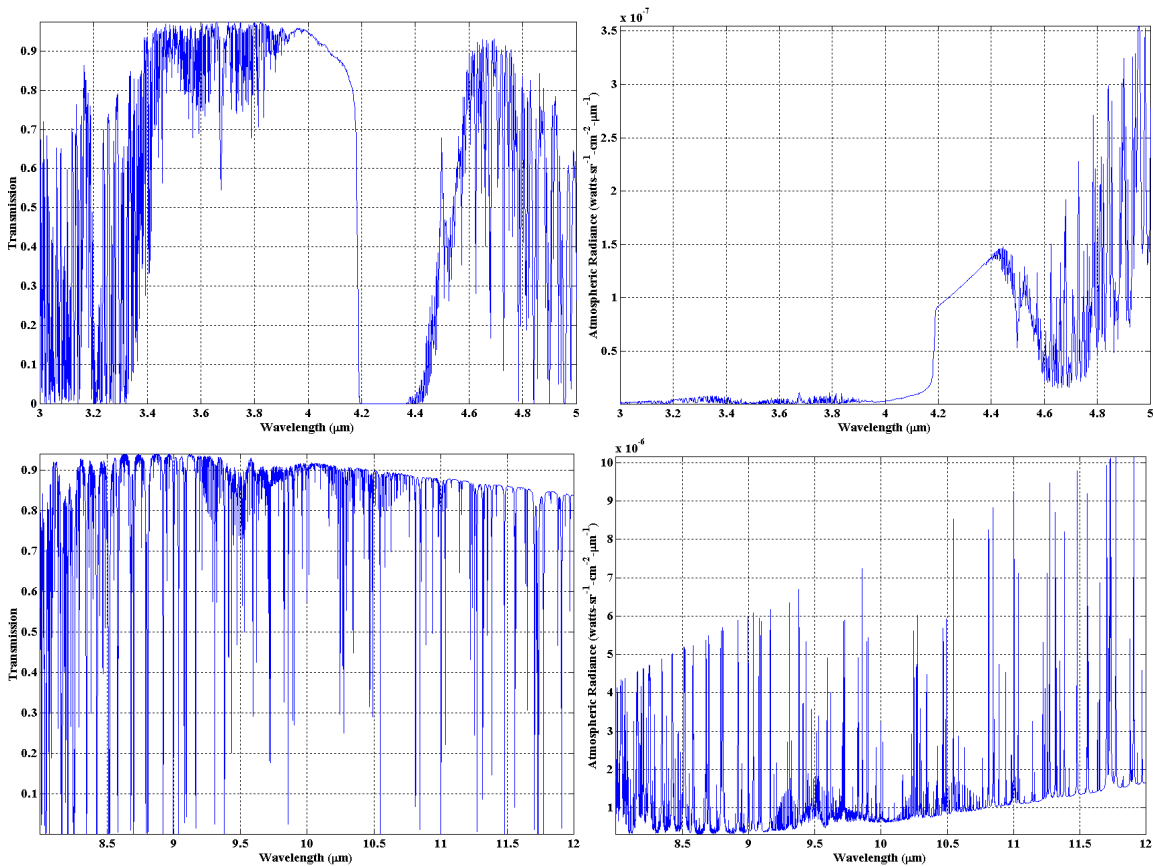
Figure A-5: MWIR/LWIR spectral atmospheric windows and path radiances for Scenario #5. Conditions are listed in Table A-5.

Appendix B Generic Normalized System Input Responses
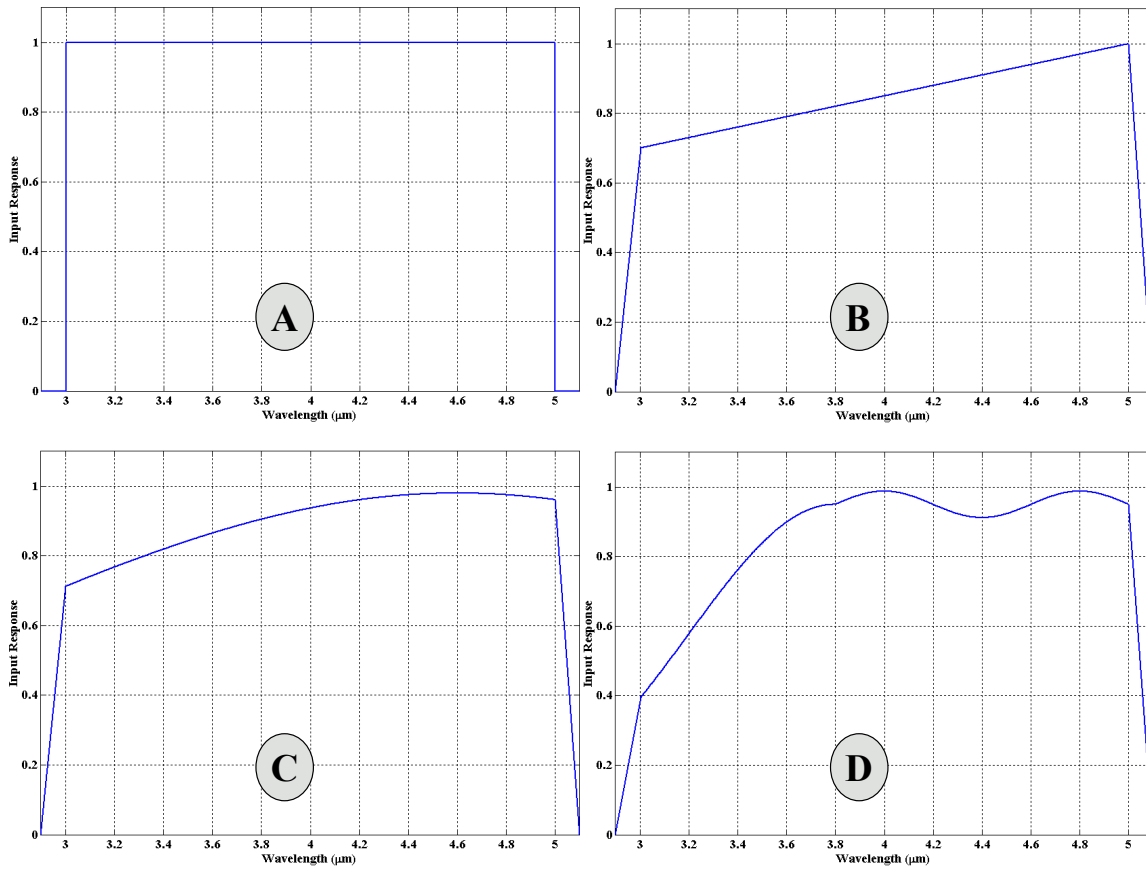
Figure B-1: The four generic normalized system input responses available through the graphical user interface. These generic responses are the same for the longwave IR band. **A:** The ideal response is rectangular window with a magnitude of one. **B,C:** These filters are similar to an indium antimonide detector at MWIR as shown in Figure 3-30. **D:** This response is just a generic fictional response. Actual input responses at each of the IR bands can be added to the radiometric model.

Appendix C Aircraft Parts Breakdown
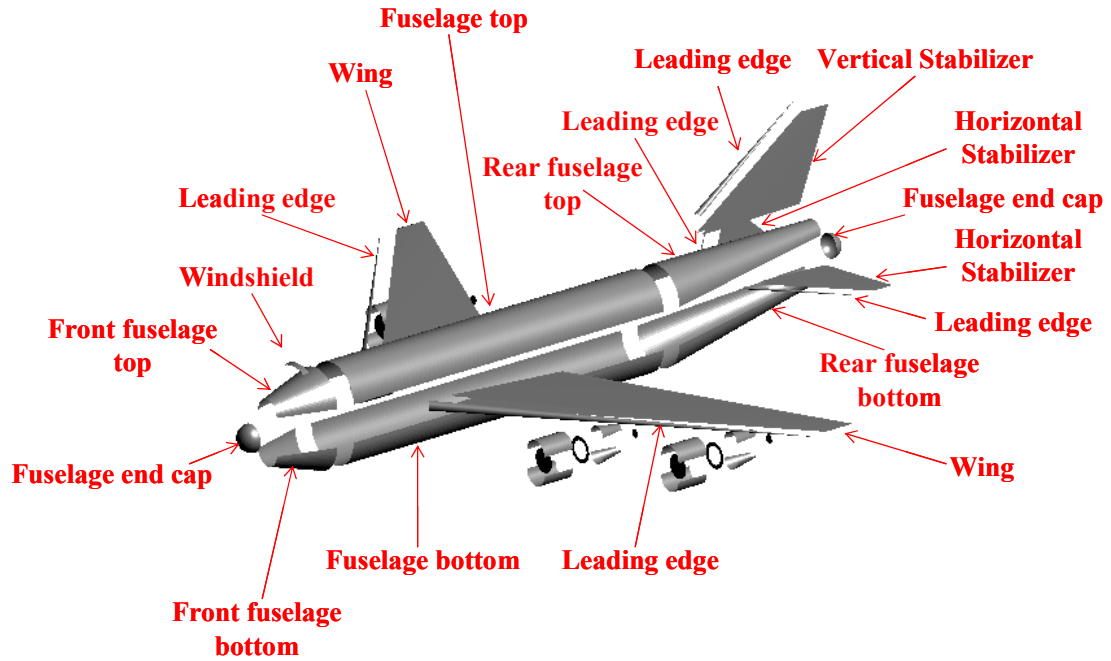
Figure C-1: The complete aircraft parts breakdown. The complete engine breakdown is shown in Figure 3-6.

Bibliography

[1] Boeing 747-400, *Airplane Characteristics for Airport Planning*, Document No D6-58326-1, Boeing Commercial Airplanes, 2002

[2] Bolkcom C., Elias B., and Feickert A. *Homeland Security: Protecting Airliners from Terrorist Missiles.* Congressional Research Service (CRS) Report for Congress, 2003.

[3] "Briton arrested by the FBI over missile smuggling," *The Financial Times*, 8 (16 Aug 2003).

[4] Cheng D. K., *Field and Wave Electromagnetics*, Reading MA, Addison-Wesley Publishing, 1989

[5] Correspondence with Dr. Joe Costantino, AFRL/MLBT, Optical Measurement Facility, dated December 10, 2004

[6] Dereniak E. and Boreman G. *Infrared Detectors and Systems.* New York: John Wiley and Sons, Inc., 1996.

[7] Gellert W., et al, *The VNR Concise Encyclopedia of Mathematics*, New York: Van Norstrand Reinhold, 1975

[8] Hecht E. *Optics* (4th Edition). San Fransisco: Addison Wesley, 2002.

[9] Hudson R. D. *Infrared System Engineering.* New York: John Wiley and Sons, Inc., 1969.

[10] Hughes D. and Dornheim M. A. "DHL/EAT Crew Lands A300 With No Hydraulics After Being Hit By Missile," *Aviation Week & Space Technology* (7 Dec 2003).

[11] Hughes D. and Wall R. "Missile Attack on DHL Jet Keeps Self-Defense Issue Bubbling," *Aviation Week & Space Technology* (30 Nov 2003).

[12] "IR Missiles Brought Down Majority of Russian Aircraft*," Journal of Electronic Defense, 23* (2):30 (Feb 2000).

[13] Magrab E. B., et al, *An Engineer's Guide to MATLAB*[®], Upper Saddle River NJ: Prentice Hall, 2000

[14] McWhethy J. "Air Force Attack Attempt Discovered," *ABC News* (12 Jun 2002).

[15] Morris T. A. *Analysis of Uncertainties in Infrared Camera Measurements of a Turbofan Engine in an Altitude Test Cell*. Air Force Institute of Technology Master's Thesis, 2004

[16] "Protecting the Big Boys: Directed IR Countermeasures for Large Aircraft," *Journal of Electronic Defense, 23* (12):47 (Dec 2000).

[17] Simon, H. "Funding Remains At Center Of Debate On Missile Defense For Airliners," *Aviation Week & Space Technology* (28 Apr 2004).

[18] Spolar C. "Israeli passengers stunned by news of attack," *Chicago Tribune* (28 Nov 2002).

[19] "Stingers and a sting: Arms smuggling," *The Economist (US),* 368 (8337):26 (16 Aug 2003).

[20] Thomas G. B, and Finney R.L, *Calculus and Analytic Geometry*., Reading MA: Addison-Wesley Publishing Company, 1992

[21] "Understanding the infrared threat," *Journal of Electronic Defense, 22* (2):35 (1999).

[22] Wolfe W. L. and Zissis G. J., editors. *The Infrared Handbook* (4th Edition). IRIA Series in Infrared and Electro-Optics, Environmental Research Institute of Michigan, 1993

REPORT DOCUMENTATION PAGE

1. REPORT DATE (DD-MM-YYYY) 09-03-2005	2. REPORT TYPE **Master's Thesis**	3. DATES COVERED (From – To) Apr 2004 – Mar 2005

4. TITLE AND SUBTITLE MODELING THE INFRARED INTENSITY OF A LARGE COMMERICAL AIRCRAFT	5a. CONTRACT NUMBER
	5b. GRANT NUMBER
	5c. PROGRAM ELEMENT NUMBER
6. AUTHOR(S) Martinez, Ruben, Captain, USAF	5d. PROJECT NUMBER
	5e. TASK NUMBER
	5f. WORK UNIT NUMBER

7. PERFORMING ORGANIZATION NAMES(S) AND ADDRESS(S) Air Force Institute of Technology Graduate School of Engineering and Management (AFIT/EN) 2950 Hobson Way WPAFB OH 45433-7765	8. PERFORMING ORGANIZATION REPORT NUMBER AFIT/GE/ENP/05-01
9. SPONSORING/MONITORING AGENCY NAME(S) AND ADDRESS(ES) AFRL/SNS Attn: George R. Simpson 2951 K Street DSN: 785-9288 WPAFB OH 45433 email: George.Simpson@wpafb.af.mil	10. SPONSOR/MONITOR'S ACRONYM(S)
	11. SPONSOR/MONITOR'S REPORT NUMBER(S)

12. DISTRIBUTION/AVAILABILITY STATEMENT

APPROVED FOR PUBLIC RELEASE; DISTRIBUTION UNLIMITED

13. SUPPLEMENTARY NOTES

14. ABSTRACT

Measuring the infrared signature of large civilian aircraft has become increasingly important due to the proliferation of man-portable air defense systems (MANPADS) and the increasing threat of their use by terrorists. Because of the range of these shoulder-fired weapons, most aircraft flying over 20,000 feet are safe from the threat; however, aircraft taking-off or landing are extremely vulnerable.

A radiometric model was developed to simulate a large commercial aircraft's infrared intensity during these two critical phases of flight. The radiometric model was largely based on the dimensions of a Boeing 747-400 aircraft. It is capable of simulating elevation angles between -20º and +20º, as well as 360º in azimuth in its projected area analysis of the faceted model. The model utilizes an obscuration matrix to determine which parts of the aircraft are in view by the observer and thus contribute to the aircraft's intensity. A simple one-bounce reflection matrix was also included to incorporate reflections of hot parts off other body parts, as well as earth- and sky-shine contributions to the overall intensity. Various atmospheric scenarios can be loaded into the model to incorporate atmospheric transmittance and radiance effects in the simulation. Measurements taken at the Air Force Research Laboratory's Optical Measurement Facility are used to create material matrices which account for angle-dependent emissivity and reflectance.

A graphical user interface (GUI) was developed to allow a user to change variables and view the resultant aircraft intensity as a function of elevation and azimuth angles. A graphical output of the faceted model assists in visualizing aircraft hot parts, reflections, and/or obstructed parts to identify significant contributions to the aircraft's infrared intensity.

15. SUBJECT TERMS
Infrared radiation, infrared optical systems, infrared research, infrared signatures, infrared spectra, commercial aircraft, airliners, passenger aircraft, aircraft models, mathematical models

16. SECURITY CLASSIFICATION OF:			17. LIMITATION OF ABSTRACT	18. NUMBER OF PAGES	19a. NAME OF RESPONSIBLE PERSON Dr. Michael A. Marciniak (ENP)
REPORT U	ABSTRACT U	c. THIS PAGE U	UU	94	19b. TELEPHONE NUMBER (Include area code) (937) 255-3636, X4529; e-mail: Michael.Marciniak@afit.edu